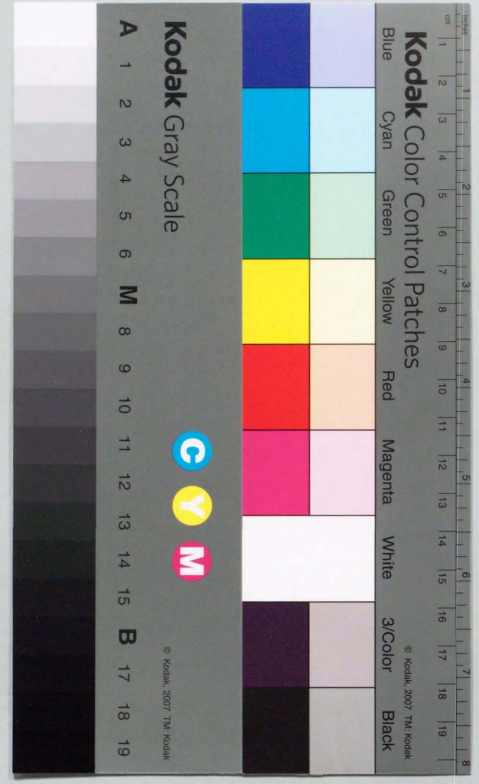

THESIS

A spectroscopic study of the metal-insulator transition in perovskite-type manganites

ペロブスカイト型マンガン酸化物の金属-絶縁体転移の分光学的研究

Yoichi Okimoto
沖本洋一
Department of Physics, University of Tokyo

1998

THESIS

A spectroscopic study of the metal-insulator transition in perovskite-type manganites

ペロブスカイト型マンガン酸化物の金属-絶縁体転移の分光学的研究

Yoichi Okimoto
沖本洋一
Department of Physics, University of Tokyo

1998

Contents

Chapter 1

Introduction

1.1 Physical properties of the double-exchange conducting ferromagnet and historical background

The hole-doped manganese oxides with perovskite-type structure have long been known as one of prototypical conducting ferromagnets [1, 2, 3]. The ferromagnetic metallic state in these compounds is stabilized by the double-exchange mechanism [4, 5, 6] originating from the strong coupling between the charge-carriers and local spins which are both dominantly of the $3d$ orbital character. In the course of the recent renaissance of study on the $3d$ transition metal oxides, these double-exchange systems have been revisited and their new aspects are being unraveled. Those are versatile intriguing phenomena induced by a magnetic field, such as 'colossal' magnetoresistance (CMR) observed commonly near the ferromagnetic transition temperature (T_c) in the most of the doped manganites [7, 8, 9, 10, 11, 12, 13, 14], the field-melting of the charge/orbital-ordered state accompanying a huge change of the resistivity [15, 16, 17, 18], and field-induced structural transitions even near room temperature [19, 20], field-control of intergrain or interplane tunneling of highly spin-polarized carriers [21, 22], and so on. All these phenomena are considered as relevant to unique electronic structures of the perovskite-type manganites in which mutual coupling among the charge, spin, orbital and lattice degrees of freedom is particularly important.

The parent material $LaMnO_3$ is a charge-transfer type (CT-type) insulator [23, 24] in the Zaanen-Sawatzky-Allen scheme [25], and has four d-electrons per Mn^{3+} site with a

configuration of $t_{2g}^3 e_g^1$. As the nominal hole concentration (x) is increased, $La_{1-x}Sr_xMnO_3$ shows a magnetic- and structural-phase transition form antiferromagnetic to ferromagnetic state around $x = 0.1$ and subsequently the low-temperature ferromagnetic phase undergoes an insulator-to-metal transition around $x = 0.17$. The crystal structure is also transformed from an orthorhombic to rhombohedral form with hole-doping ($x \approx 0.17$), as shown in Fig. 1.1 [19]. Figure 1.2 shows the magnetic- and strucural-phase diagram in $La_{1-x}Sr_xMnO_3$ [36] derived by neutron diffraction measurements. According to the phase diagram, this system has two orthorhombic phases; one is the conventional distorted perovskite-type orthorhombic phase (O^*) and the other largely distorted one (O') due to the static Jahn-Teller (JT) effect.

A conducting ferromagnetic state realized with the hole doping is explained by the double-exchange mechanism [4, 5, 6]. In the metallic phase, the conduction band consists of $3d$ e_g state hybridized strongly with the O $2p$ state while the t_{2g} electrons are still localized forming local spins ($S = 3/2$). The strong interaction (Hund's-rule coupling) between an e_g electron and a t_{2g} local spin plays an important role in the electronic properties of this system. Recently, such a strongly spin-charge coupled state has been extensively studied in the light of the observation of a colossal magnetoresistance (MR) effect. Figure 1.3 shows one of the examples for such MR effects in $La_{1-x}Sr_xMnO_3$ crystals [14]. As a model in the doped manganites, Kubo and Ohata [26] proposed the following Kondo lattice model with ferromagnetic exchange coupling ($J_H > 0$):

$$H = -\sum_{i,j,\sigma} t_{i,j} \left(C_{i,\sigma}^{\dagger} C_{j,\sigma} + \text{H.c.} \right) - J_H \sum_i \vec{s}_i \cdot \vec{S}_i \qquad (1.1)$$

Here, $\vec{s}_i$ represents the spin of the itinerant e_g electron and $\vec{S}_i$ the localized t_{2g} spin ($S = 3/2$). The Hund's-rule coupling energy SJ_H (≈ 2 eV [23]) exceeds the one-electron bandwidth (W) [27]. A consequence of this strong electron-spin coupling is the exchange-splitting of the spin-polarized conduction bands by $\approx SJ_H$ and the spin-polarization of the conduction electrons varies from 0 to 100 % with lowering temperature. Recently, Furukawa [28, 29] has derived the optical conductivity from this Kondo lattice model

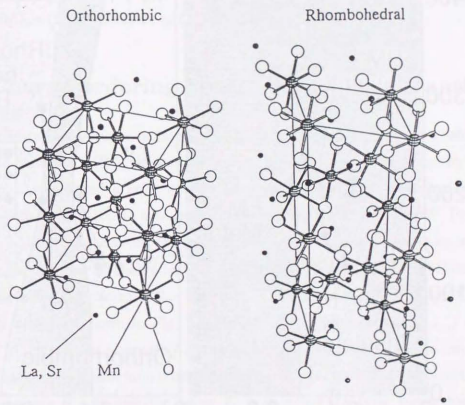

Figure 1.1: Schematic crystal structures of $La_{1-x}Sr_xMnO_3$ in the orthorhombic phase ($Pbnm$) and rhombohedral phase ($R3\bar{c}$).

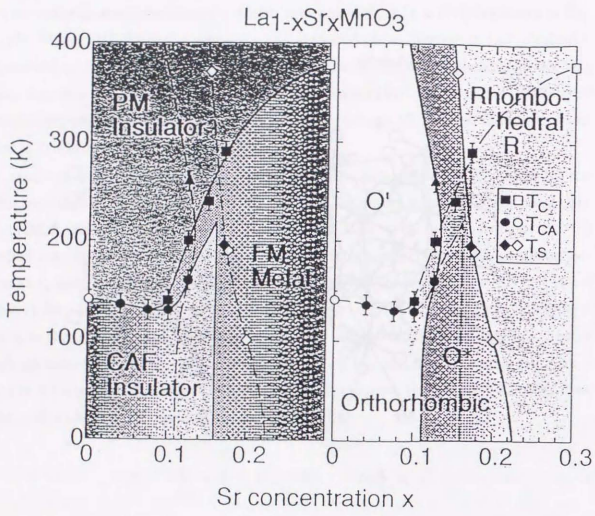

Figure 1.2: Magnetic- (left panel) and structural- (right panel) phase diagram of $La_{1-x}Sr_xMnO_3$ (from Ref. [36]).

by the dynamical mean-field approximation, and showed that the spectra are critically dependent on the spin-polarization accompanying the spectral weight transfer from the interband transitions between the exchange-split bands to the Drude part, as shown in Fig. 1.4. Therefore, the optical spectroscopy in the photon energy region up to above $\approx SJ_H$ is indispensable to clarify the spin-polarization dependent electronic features in $La_{1-x}Sr_xMnO_3$. We spectroscopically investigate the variation of electronic structure in $La_{1-x}Sr_xMnO_3$ with temperature and the hole doping (x) in chapter 3.

1.2 Charge-ordering/disordering phase transition

As mentioned in the previous section, $La_{1-x}Sr_xMnO_3$ system, which has a relatively wide one-electron bandwidth (W), shows a ferromagnetic metallic state mediated by the double-exchange mechanism and a large magnetoresistance (MR) effect was observed near the Curie temperature (T_c) [10]. In a more distorted perovskite with a smaller W, $Pr_{1-x}Ca_xMnO_3$ ($0.3 \leq x \leq 0.5$) system, however, the metallic (and ferromagnetic) state is no more present and real space ordering of charge carriers (charge ordering) takes place below the charge ordering transition temperature T_{co}. Below T_{co}, the nominal Mn^{3+} and Mn^{4+} species are regularly arranged as shown in Fig. 1.5. Upon the charge ordering, $d_{3x^2-r^2}$ and $d_{3y^2-r^2}$ orbitals at Mn^{3+} site are alternately ordered in the ab-plane [30]. As the temperature is decreased, antiferromagnetic spin ordering subsequently occurs below the Neel temperature (T_N). The pattern of spin ordering below T_N is so called CE-type, but a direction of an easy axis of sublattice magnetization is different with hole doping concentration x. As seen in Fig. 1.5, the angle between the easy axis of magnetization and b-axis is increased from 0° with the decrease of x from 1/2, and spins are finally ordered ferromagnetically along c-axis at x=0.3. Such ferromagnetic spin ordering occurs probably because extra electrons ($1/2 - x$) arising from the incommensurate doping ($x \neq 1/2$) occupy $d_{3d^2-r^2}$ in Mn^{4+} site and mediate the double-exchange type interaction among the t_{2g} spins along the c-axis. The fact that T_N is lower than T_{co} is characteristic of $Pr_{1-x}Ca_xMnO_3$ system and contrary to the case of $Nd_{1/2}Sr_{1/2}MnO_3$ system where the similar CE-type but *concomitant* spin and

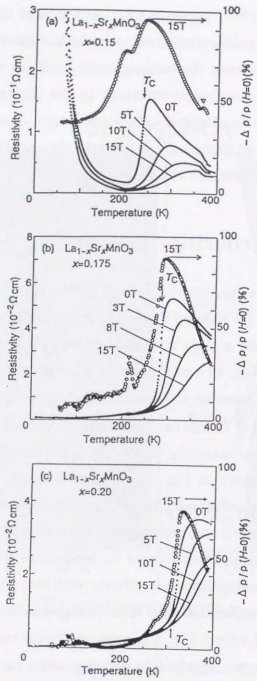

Figure 1.3: Temperature dependence of resistivity of $La_{1-x}Sr_xMnO_3$ crystals under various magnetic fields: (a) $x = 0.15$, (b) $x = 0.175$, and (c) $x = 0.20$ (from Ref. [10]).

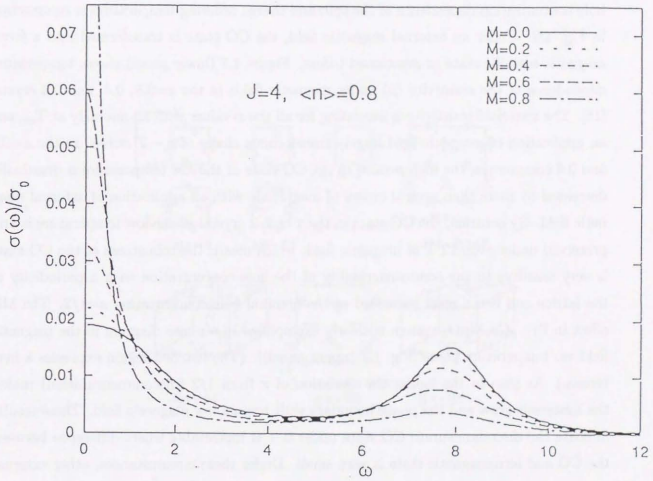

Figure 1.4: Optical conductivity spectra as a function of the spin-polarization (M) calculated by the dynamical mean-field approximation (from Ref. [28]).

charge ordering takes place [18]. With the decrease of temperature below T_N, the canted antiferromagnetic ordering takes place at a critical temperature T_{CA} for $x < 1/2$ crystal [31]. (This order is perhaps a consequence of incommensurate hole-doping level ($x < 1/2$) and in the $x = 1/2$ crystal such a canted magnetic order has not been observed.) The hole concentration dependence of the spin and charge ordering temperature is summerized in Fig. 1.6. Under an external magnetic field, the CO state is transformed into a ferromagnetic metallic state as mentioned before. Figure 1.7 (lower panel) shows temperature dependence of the resistivity (ρ) under magnetic fields in the x=0.5, 0.4, and 0.3 crystal [15]. The zero-field resistivity is insulating for all the x-values with an anomaly at T_{co}, and an application of magnetic field largely transforms a shape of $\rho - T$ curve. In the x=0.3 and 0.4 compounds, the high ρ-value in the CO state at the low temperature is drastically decreased by more than several orders of magnitude with an application of external magnetic field. By contrast, the CO state in the $x = 1/2$ crystal at the low temperature is still preserved under even 12 T of magnetic field, which means the robustness of the CO state is very sensitive to the commensurability of the hole concentration with a periodicity of the lattice and hence most enhanced at the nominal hole concentration x=1/2. The MR effect in $Pr_{1-x}Ca_xMnO_3$ system is clearly exemplified in a phase diagram in the magnetic field vs. temperature plane [Fig. 1.7 (upper panel)]. (The hatched region expresses a hysteresis.) As seen in the figure, the deviation of x from 1/2 (discommensuration) makes the hysteresis grow and the phase boundary shift toward low magnetic field. These results indicate the discommnsurate CO state under 0 T is metastable where difference between the CO and ferromagnetic state is very small. Under these circumstances, other external perturbation than the magnetic field can trigger the transition of the metastable CO state especially in the x=0.3 crystal, such as irradiation with X-ray [32], photo-excitation [33], and current-injection [20], which are all relevant to the melting of the CO state. We investigate in chapter 4 the variation of the anisotropic electronic structure of the CO state with temperature and magnetic field in terms of optical conductivity spectra.

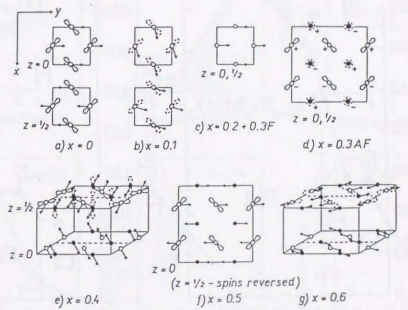

Figure 1.5: The configuration of the charge, spin, and orbital in the charge ordered state (From Ref. [30]). Open and closed circles denote Mn^{3+} and Mn^{4+}, respectively. The lobes show the orientation of d_{z^2} or d_{y^2} orbitals.

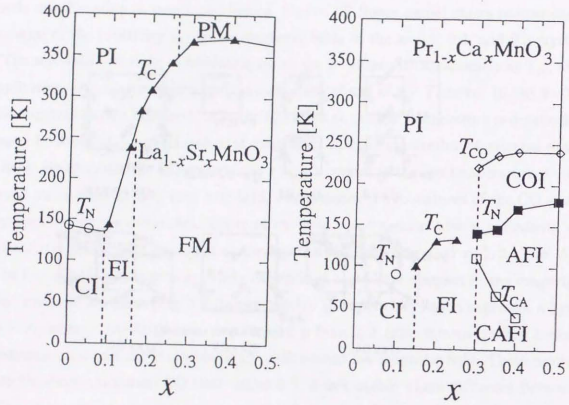

Figure 1.6: The magnetic as well as electronic phase diagram of $Pr_{1-x}Ca_xMnO_3$ (right panel) and $La_{1-x}Sr_xMnO_3$ (left panel) (from Ref. [15]).

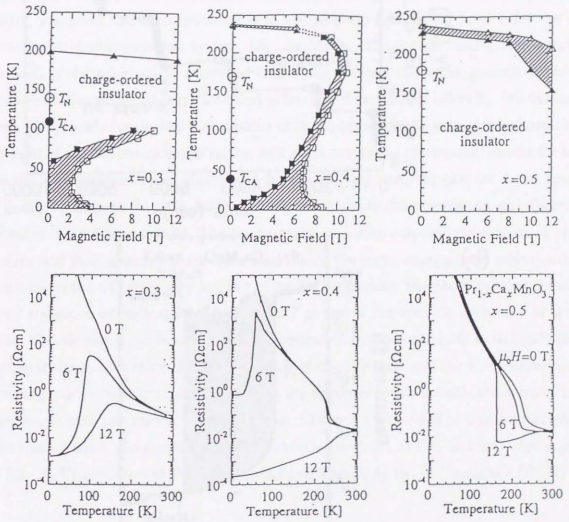

Figure 1.7: Upper panel: Electronic pahse diagram in $Pr_{1-x}Ca_xMnO_3$ in the magnetic field and temperature plane. Lower panel: Magnetic field dependence of the resistivity in $Pr_{1-x}Ca_xMnO_3$. (From Ref. [15])

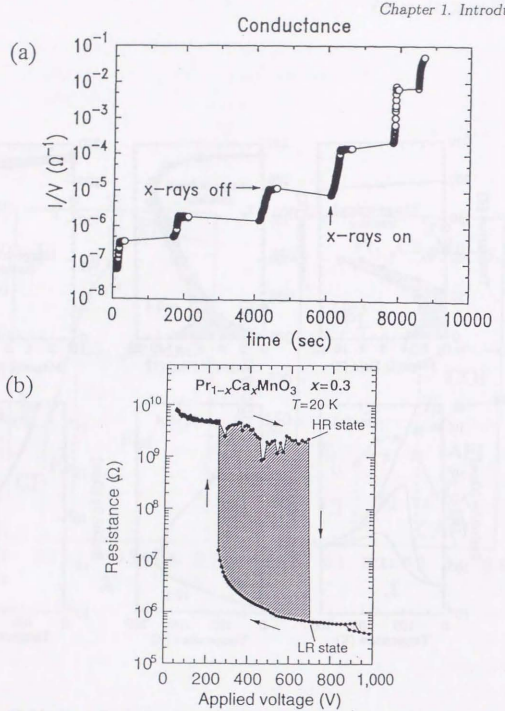

Figure 1.8: (a): X-ray induced insulator-metal transition in $Pr_{1-x}Ca_xMnO_3$ ($x = 0.3$) (From Ref. [32]). The resistance is changed with the X-ray illumination. (b): Change of resistance at 20 K as a function of applied voltage (From Ref. [20]).

1.3 Outline of this thesis

The format of this thesis is as follows: We explain in chapter 2 the experimental processes for the sample preparation and optical measurements. Chapter 3 describes optical conductivity spectra and their variation with temperature and doping level x for the most prototypical double-exchange system, $La_{1-x}Sr_xMnO_3$. The optical conductivity spectrum above T_c is characterized by interband transitions between the exchange-split conduction bands, and it gradually changes into that of intraband excitations below T_c. We discuss the large energy-scale (up to ≈ 2 eV) transfer of the spectral weight with spin-polarization in the light of the double-exchange model, and point out some experimental results for which the simple double-exchange theory can hardly give account. In chapter 4, we spectroscopcally investigate $Pr_{1-x}Ca_xMnO_3$ system, which shows charge-ordering and disordering transition with magnetic field. The temperature- and magnetic field depecdence of optical spectra and their anisotropy are elucidated taking the spin-, charge-, and orbital-ordering structure in the CO state into account. Chapter 5 describes the photo-induced insulator-metal transition under magnetic field of 1.2 T as one of the versatile properties of the CO state. The electrical conductivity and magnetization increase abruptly with irradiation of visible/IR laser, indicating the photo-melting of the CO state and the photo-generation of ferromagnetic metallic domains. We discuss the nature of such a notable phase transition in comparison with late results by other groups. Chapter 6 is devoted to concluding remarks.

In these studies, the samples of $La_{1-x}Sr_xMnO_3$ (x=0, 0.1, 0.175, and 0.3) were supplied by Mr. A. Urushibara and $Pr_{1-x}Ca_xMnO_3$(x=0.3 and 0.4) Dr. Y. Tomioka (*JRCAT*).

Chapter 2

Experimental

2.1 Sample preparation and characterization

$La_{1-x}Sr_xMnO_3$

Crystals of $La_{1-x}Sr_xMnO_3$ investigated were melt-grown by a floating zone method. The starting materials were La_2O_3, $SrCO_3$, and $MnCO_3$. La_2O_3 was fired in air at 1200C° for 12 hours before use. $MnCO_3$ was also calcined in air at 1200C° for 12 hours to form Mn_3O_4, which is the most stoichiometric compound in the Mn-O systems. Then, the raw materials were weighted to a prescribed ratio, mixed and stirred with acetone for 1 hours in a ball mill. The mixture was heated at 1200C° for 24 hours in air. The prereacted materials ware then pulverized and mixed again. After this process, the feed rods was formed to a cylindrical shape of about 5 mm in diameter and 80 mm in length with pressure of 2 ton/cm^2 and heated at 1200C° in air for 12 hours. The apparatus used for the crystal growth was a floating zone (FZ) furnace equipped with two halogen incandescent lamps and hemielliptic focusing mirrors. The feed and seed rods were rotated in opposite directions at a relative rate of 50 rpm and the melted zone was vertically scanned at a speed of 8-10 mm/h. The atmosphere during the crystal growth was changed with the crystal composition; in flow of argon gas for x=0, air for x=0.1,0.175, and mixture of an oxygen and an argon gas for x=0.3.

Measurements of powder X-ray diffraction patterns showed that all the obtained samples

were of single phase and that the crystal structure at room temperature were orthorhombic ($x = 0, 0.1$, and 0.175) and rhombohedral ($x = 0.3$). Analyses of chemical composition were performed for each sample using an electron probe microanalyzer (EPMA) and redox titration, and showed the almost identical composition with the prescribed ratio [14]. To characterize the compounds, we have measured temperature dependence of resistivity and magnetic susceptibility. For the resistivity measurements, the samples were cut to a rectangular shape and a standard four-probe technique was used. Magnetic susceptibility was measured with a superconducting quantum interference device (SQUID) magnetometer.

$Pr_{1-x}Ca_xMnO_3$

A crystal of $Pr_{1-x}Ca_xMnO_3$ ($x = 0.3$, 0.4) was also grown by the floating zone method. Mixed powder of Pr_2O_3, $CaCO_3$, and Mn_3O_4 with a prescribed ratio was first calcined at 1050°C in air for 24–48 hour and pressed into a rod (about 150 mm in length and 7mm in diameter). Inductively coupled plasma atomic emission (ICP) spectroscopy and chemical titration have confirmed that the obtained crystal has precisely prescribed stoichiometry.

2.2 Optical measurements

Optical measurements: Temperature dependence

We measured Reflectivity spectra ($R(\omega)$) over a wide photon energy region (0.01–36 eV) at room temperature. Typical sizes of crystals of $La_{1-x}Sr_xMnO_3$ ($x = 0$, 0.1, 0.175, and 0.3) and $Pr_{1-x}Ca_xMnO_3$ ($x = 0.4$) are $\approx$6×6×1 mm^3 and $\approx$4×5×0.5mm^3, respectively. The orthorombic or rhombohedral distortion of perovskite-type manganites is not so large that we neglected polarization dependence of $R(\omega)$ in $La_{1-x}Sr_xMnO_3$. In $Pr_{1-x}Ca_xMnO_3$ system, however, it is impossible to neglect the anisotropy of $R(\omega)$ mainly due to the charge, spin, and orbital ordering as mentioned before, so that we measured $R(\omega)$ on the [1 0 0] face of the x=0.4 crystal (*Pbnm* orthorhombic structure) and investigated the difference of *b*- and *c*-axis polarized $R(\omega)$. We show in Table. 2.1 the optical system for certain photon energy ranges.

Energy (eV)	Monochromator	Detector	Light source	Polarizer
0.01–0.08	Fourier-transfer type	Si bolometer	Glober lamp	Wire grid
0.06–0.8	Fourier-transfer type	HgCdTe	Glober lamp	Wire grid
0.6–1.5	grating type	InAs	halogen lamp	Calcite
1.2–3	grating type	Si	halogen lamp	Calcite
2.4–5	grating type	Si	Xe lamp	Calcite
4–36	Seya-Namioka type	photomultiplier	synchrotron radiation	synchrotron radiation

Table 2.1: The way of measuring reflectivity at specific photon-energy ranges in the present experiments.

In order to investigate the temperature dependence of the optical spectra, we measured reflectivity spectra at selected temperatures up to 3.0 eV. As a reference mirror, we used evaporated Au film (far–near-infrared region), and Ag film (visible range). We fixed the reference mirror near the sample within a cryostat and interchanged with the sample. Namely, all the spectra were measured at each temperature from 0.01 eV to 3 eV and extrapolated by the data above 3 eV at room temperature. Such a procedure is possible and reasonable because the variation of the reflectivity in the high-energy region with the change of the temperature is negligibly small (less than 1 % at 3.0 eV).

Optical spectrum: Magnetic field dependence

For $Pr_{1-x}Ca_xMnO_3$ (x=0.4) crystal, we measured the magnetic field dependence of $R(\omega)$ at 30 K besides the temperature dependence. (Under 0 T, the temperature dependence of $R(\omega)$ was investigated between 0.01 eV and 3 eV like $La_{1-x}Sr_xMnO_3$ system.) High magnetic field measurements of $R(\omega)$ between 0.05 eV and 3 eV at 30 K were made with a 7 T split-type superconducting magnet (Oxford) equipped with optical windows for infrared and visible spectroscopy. The magnetic field was applied along the *b*-axis of the *Pbnm* orthorhombic lattice. We measured $R(\omega)$ under Voigt-geometry ($\mathbf{k}\perp\mathbf{H}$) for 0.05 eV−0.8 eV and Faraday-geometry ($\mathbf{k}\perp\mathbf{H}$) 0.6 eV−3 eV.

It is worth noting here that external magnetic field gives birth to various magneto-optical effects e.g., Kerr or Faraday effect, which are due to anisotropy caused by external magnetic field. Under these circumstances, an off-diagonal component of dielectric tensor ($\epsilon_{xy}(\omega)$)

Energy (eV)	Light source	Windows of the magnet	Geometry
0.06 eV–0.8 eV	Nichrome wire	KRS-5 and ZnSe	Voigt
0.6 eV–3 eV	halogen lamp	Quartz	Faraday

Table 2.2: The way of measuring reflectivity at specific photon-energy ranges under magnetic field. Monochromators and light sources are the same as the case for the temperature dependence-measurements. (see Table 2.1.)

plays an essentially important role. As for the manganese oxide, however, the magnitude of such $\epsilon_{xy}(\omega)$ in the low-energy (< 4 eV) region is much smaller than that of diagonal part due partly to no orbital moment for the e_g-electron and hence to minimal spin-orbit coupling [34], so that we may neglect the contribution of $\epsilon_{xy}(\omega)$ in executing K-K analysis (*vide infra*).

The details of the optical system between certain energy ranges are summerized in Table 2.2.

2.2.1 Kramers-Kronig transformation

In this section, we explain a procedure to obtain the complex dielectric function ($\epsilon(\tilde{\omega})$) from $R(\omega)$. To calculate the $\epsilon(\tilde{\omega})$, it is essential to acquire information of phase shift ($\theta(\omega)$) besides the $R(\omega)$ which is obtained experimentally. These two quantities ($\theta(\omega)$ and $R(\omega)$) are not independent but correlated with each other by a Kramers-Kronig relation as following:

$$\theta(\omega) = -\frac{\omega}{2\pi} P \int_0^\infty \frac{\ln R(s)}{s^2 - \omega^2} ds. \tag{2.1}$$

When we executed a numerical calculation of Eq. (2.1) in practice, we assumed the constant reflectivity ($R \propto \omega^0$) below 0.01 eV and Drude-type ($R \propto \omega^{-4}$) extrapolation above 36 eV. The $R(\omega)$ and the $\theta(\omega)$ are connected with the $\epsilon(\tilde{\omega})$ as follows;

$$\sqrt{R(\omega)}\exp(i\theta) = \frac{\sqrt{\tilde{\epsilon}(\omega)} - 1}{\sqrt{\tilde{\epsilon}(\omega)} + 1}. \tag{2.2}$$

Thus, we can obtain both the real and imaginary part of the $\tilde{\epsilon}(\omega)$ from the $R(\omega)$ and the $\theta(\omega)$. We also obtained the optical conductivity $\sigma(\omega)$, which is defined as following;

$$\sigma(\omega) = \frac{\omega \mathrm{Im}\tilde{\epsilon}(\omega)}{4\pi}. \tag{2.3}$$

The zero-frequency limit of $\sigma(\omega)$ should coincides with the dc conductivity.

2.3 Photo-induced insulator-metal transition

We investigated the photo-induced insulator-metal transition for $Pr_{0.7}Ca_{0.3}MnO_3$crystal and explain the experimental procedure in this section. For the resistivity measurements, the x=0.3 crystal was set within the split-type sperconducting magnet (Oxford), and a probe used in this experiment is shown in Fig. 2.1. Temperature and magnetic field were maintained at 30 K and 1.2 T all through the measurements. Electrodes were formed by evaporation of gold onto the surface of the crystal and the distance of the electrodes was $\approx 75\mu$m. For the photo-excitation, we used a pulsed Nd-YAG laser (wavelength 532 nm) with 5 ns in duration, and $\approx 30\mu$ J/mm^2. A pulsed laser was introduced into the magnet through a malti-channel optical fiber and irradiated to between the electrodes on the sample. (see Fig. 2.1.) For the measurements of the magnetization, we utilized a superconducting quantum interference device (SQUID) magnetometer. A pulsed laser also introduced into the SQUID through an optical fiber was illuminated to the x=0.3 compound at 30 K and 1.2 T. The sample was fixed just below the optical fiber using plastic resin. The magnitude of the diamagnetization of the optical fiber or the resin is negligibly small compared with that of the magnetization of the sample (canted ferromagnetism).

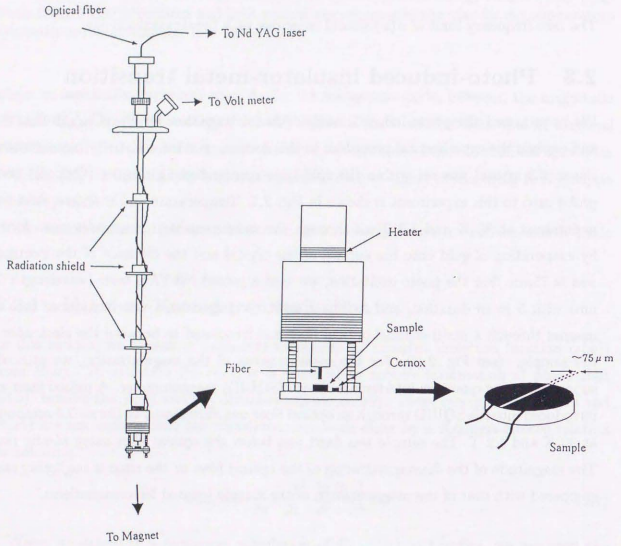

Figure 2.1: Probe with optical fiber for the measurement of photo-induced insulator-metal transition under magnetic field.

Chapter 3

Variation of electronic structure in $La_{1-x}Sr_xMnO_3$ ($0 \leq x \leq 0.3$) studied by optical conductivity spectra

3.1 Introduction

In this chapter, we investigate the optical spectra of $La_{1-x}Sr_xMnO_3$ which is the most prototypical double-exchange system and discuss the variation of the electronic structures with temperature and hole-doping level (x). To overview the electronic properties of the manganites of which we measured optical spectra, we show in Fig. 3.1 the temperature dependence of resistivity (ρ) in $La_{1-x}Sr_xMnO_3$ ($x = 0, 0.1, 0.175$, and 0.3) together with the electronic phase diagram. $LaMnO_3$ ($x = 0$) is a correlated insulator with layer-type (A-type) antiferromagnetic spin structure [35, 36]. As the nominal hole concentration x increases, the ferromagnetic phase shows up and the Curie temperature T_c increases as indicated in the resistivity curve (the lower panel of Fig. 3.1) by arrows. In the region of $x \geq 0.1$, cusp structures appear in the $\rho - T$ curve around T_c. At $x = 0.1$, the $\rho - T$ curve shows an insulating behavior ($d\rho/dT < 0$) apart from the temperature region immediately below T_c, and most of the ferromagnetic phase [37] remains insulating. By contrast, the resistivity for $x \geq 0.17$ shows a metallic behavior ($d\rho/dT > 0$) below T_c. The resistivity of the metallic state at the lowest temperature is two orders of magnitude smaller than that around T_c. There is a difference between $x = 0.175$ and $x = 0.3$ in the resistivity above T_c.

The $x = 0.175$ crystal shows a semiconducting ($d\rho/dT < 0$) behavior above T_c, which is perhaps due to the combination effect of the spin scattering in the paramagnetic state and some random potential scattering [46] or dynamic Jahn-Teller coupling [47]. For $x = 0.3$, however, the $\rho - T$ curve shows a metallic behavior over the whole temperature region.

3.2 Overall features of optical spectra

First, let us overview the optical spectra of $La_{1-x}Sr_xMnO_3$ in a wide photon energy region. Arima and Tokura [38] have recently investigated the optical spectra of a series of $LaMO_3$ (M being $3d$ transition metal elements) and revealed the character of optical transitions in the respective spectra. In the following, we refer to their assignments for the interpretation of the higher-lying transitions in $La_{1-x}Sr_xMnO_3$.

We show in Fig. 3.2 the ϵ_2 spectra deduced by Kramers-Kronig analysis. As for the structures above 6 eV, there are three major peaks around 25 eV, 17 eV, and 8 eV in the ϵ_2 spectra for all the x-values.

The $\approx$ 25 eV structure marked with open triangles can be assigned to the intraatomic transition between La $5p$ and $5d$. This transition was observed to show a systematic variation with the rare earth element R, as observed in other perovskite series, $RNiO_3$ [38] and $RCoO_3$[40]. The structures around 17 eV (open squares) and 8 eV (closed triangles) correspond to interband transitions from O $2s$ to Mn $3d$ and from O $2p$ to La $5d$, respectively [38]. These assignments are consistent with those based on the photoemission and X-ray (O $1s$) absorption spectra of $La_{1-x}Sr_xMnO_3$ by Saitoh *et al.* [24]. In contrast to these x-independent features of higher-lying (> 8 eV) transitions, the lower energy part of ϵ_2 shows a large variation with the hole concentration x.

To scrutinize the changes in the lower-lying transitions, we show in Fig. 3.3 the optical conductivity spectra ($\sigma(\omega)$) at 9 K in $La_{1-x}Sr_xMnO_3$ ($x = 0 - 0.3$) in the photon energy region of 0–6 eV. The 9 K spectra are viewed as representing the ground state feature for the respective doping (x)-levels.

The $\sigma(\omega)$ spectrum of the end insulator $LaMnO_3$ (a solid line) has two notable optical

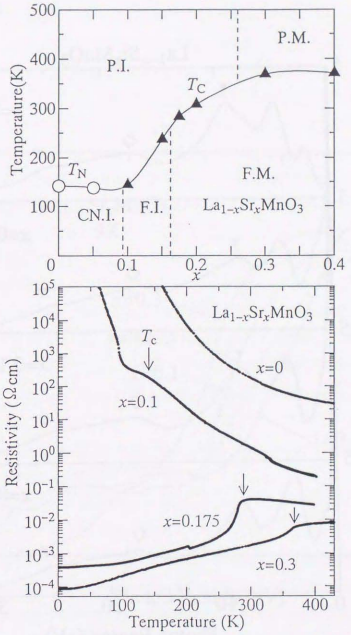

Figure 3.1: Upper panel: Electronic phase diagram of $La_{1-x}Sr_xMnO_3$ after Urushibara *et al*[14]: P.I. (paramagnetic insulator), CN.I. (spin-canted insulator), F.I. (ferromagnetic insulator), P.M. (paramagnetic metal), and F.M. (ferromagnetic metal). Lower panel: Temperature dependence of resistivity in crystals of $La_{1-x}Sr_xMnO_3$ ($x = 0$, 0.1, 0.175, and 0.3), for which the optical spectra were measured. Arrows indicate the respective Curie temperature T_c.

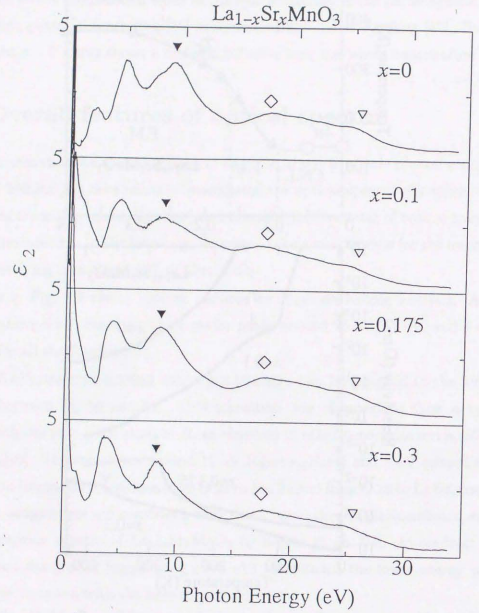

Figure 3.2: ϵ_2 (imaginary part of dielectric constant) spectra in $La_{1-x}Sr_xMnO_3$ (x = 0.1, 0.175, and 0.3) at 9 K. (The spectra above 3.0 eV were measured at room temperature, and connected to these at 9 K.)

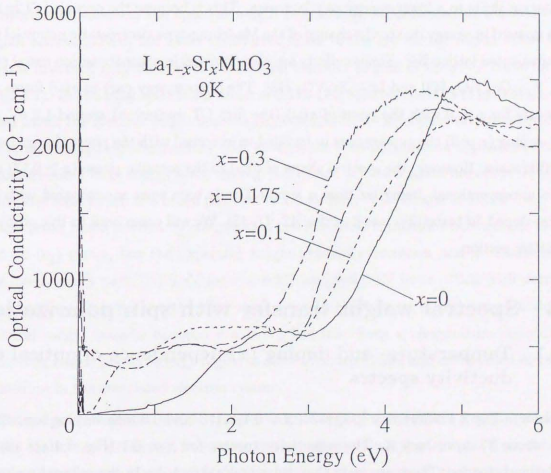

Figure 3.3: Optical conductivity spectra in $La_{1-x}Sr_xMnO_3$ (x = 0.1, 0.175, and 0.3) at 9 K. (The original reflectivity spectra above 3.0 eV, being nearly independent of temperature, were measured at room temperature, and connected to those at 9 K. See text.)

excitations around $\approx$ 1.7 eV and $\approx$ 3.0 eV. The shape of the spectrum nearly agrees with that measured by Arima *et al.* at room temperature [23, 38]. They assigned these structures to charge-transfer (CT) gap excitations, $t_{2g}^3 e_g^1 \rightarrow t_{2g}^3 e_g^2 \underline{L}$ (the lower-energy band) and $t_{2g}^3 e_g^1 \rightarrow t_{2g}^4 e_g^1 \underline{L}$ (the higher-energy one), and estimated the Hund's-rule coupling energy $J_{\rm H}$ between an e_g electron and a t_{2g} spin ($SJ_{\rm H} \approx 2$ eV) [38]. The onset of the second CT excitation shifts to a lower energy as x increases. This is because the occupied O $2p$ states shift upward in energy due to the change of the Madelung-type electrostatic potential in the Sr-substituted lattice [39]. Similar effects are also observed in other transition metal oxides, e.g., $Y_{1-x}Ca_xTiO_3$ [42] and $La_{1-x}Sr_xVO_3$ [43]. The lower-energy part in $\sigma(\omega)$ forms a gap structure for $x = 0$ with the onset of $\sigma(\omega)$ (the first CT excitation) around 1.2 eV. With hole-doping ($x \neq 0$) the gap appears to be filled-in in accord with the phase change into the metallic state. However, the spectral shape of $\sigma(\omega)$ in the metallic phase ($x \geq 0.17$) seems to be unconventional, being far from a simple Drude type even as compared with other carrier-doped $3d$ transition metal oxides [42, 41, 45]. We will come back to this problem in the latter section.

3.3 Spectral weight transfer with spin polarization

3.3.1 Temperature- and doping (x)-dependence of optical conductivity spectra

We show in Fig. 3.4 reflectivity spectra for $x = 0.1, 0.175$, and 0.3 with varying temperature from above T_c down to 9 K. The reflectivity spectra for $x = 0.1$ (Fig. 3.4(a)) show an insulating behavior: There are more than three spiky structures in the infrared region due to the optical phonon modes. With decrease of temperature the reflectivity around 0.3 eV gradually increases, but little change occurs in the far-infrared region below 0.06 eV. On the contrary, the spectra for $x = 0.175$ (Fig. 3.4(b)) and 0.3 (Fig. 3.4(c)) show a large variation with temperature. For the both compositions, the respective spectra above T_c seem to be rather characteristic of insulators with distinct optical phonon structures, but with decrease of temperature the low-energy part of reflectivity spectra evolves and finally turns into a metallic high-reflectivity band.

To investigate the electronic structure quantitatively, we derived optical conductivity spectra $\sigma(\omega)$ by the Kramars-Kronig analysis. We show in Fig. 3.5 the temperature dependence of $\sigma(\omega)$ for $x = 0.1, 0.175$, and 0.3. In the $x = 0.1$ spectra (Fig. 3.5(a)), there is little spectral weight below 0.2 eV apart from that of the three major phonon modes. As temperature decreases, the spectral weight is gradually accumulated in the mid-infrared region around 0.3 eV, but never transferred down to the low energy region below 0.1 eV. This is in accord with the carrier localization behavior as seen in the $\rho - T$ curve for x=0.1 (Fig. 3.1). In the $\sigma(\omega)$ spectra for the $x = 0.175$ (Fig. 3.5(b)) and 0.3 (Fig. 3.5(c)), on the other hand, the spectral weight shows a large temperature-dependent variation up to above 2 eV, indicating that the quantity that governs the spin-polarization dependent electronic structure has a large energy scale. In Fig. 3.5(b) and (c), each spectrum above T_c (with no spin-polarization) forms a broad peak (at $\approx$ 1.5 eV for $x = 0.175$ and $\approx$ 1.3 eV for $x = 0.3$). These broad peaks are mainly composed of the interband transitions between the O $2p$ and Mn $3d$ (e_g) states, but their spectral weight gradually decreases and is transferred into the lower-energy part, 0–1.0 eV for $x = 0.175$ and 0–0.5 eV for $x = 0.3$, with decrease of temperature. It is noteworthy that there is a clear difference in the energy scale of the spectral weight transfer between $x = 0.175$ and 0.3. Such a temperature dependence of $\sigma(\omega)$ over a wide photon energy region is quite unconventional and reminiscent of the Mott transition in the correlated electron system.

To analyze the spectral weight transfer with change of temperature (or spin polarization of the conduction electrons), we extract the temperature-independent part from the optical conductivity spectra. In Fig. 3.5(a)–(c), the respective curves of $\sigma(\omega)$ spectra at various temperatures form an envelope as depicted by a hatched curve in the figure which is composed of the lowest-lying points of all the conductivity spectra at each photon energy. It is reasonable to consider that such a temperature-independent part stands for the 'background' interband transitions between the O $2p$ and Mn $3d$ band which are not affected by change of spin-polarization. Here, we define a reduced optical conductivity spectrum ($\tilde{\sigma}(\omega)$) by subtracting the temperature-independent part (drawn by hatching) from each

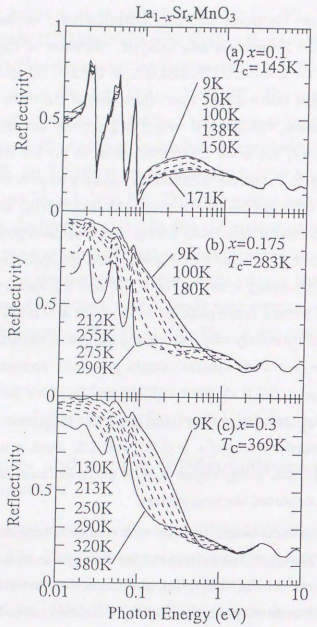

Figure 3.4: Reflectivity spectra at various temperatures in $La_{1-x}Sr_xMnO_3$; (a) $x = 0.1$, (b) $x = 0.175$, and (c) $x = 0.3$.

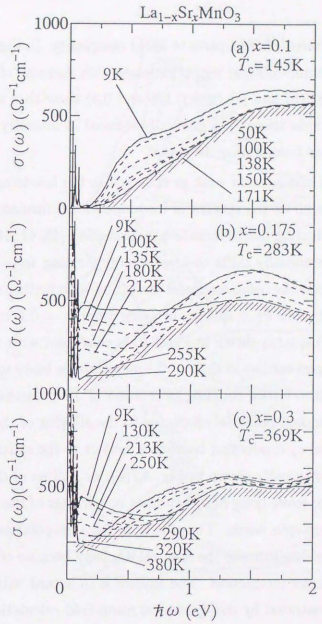

Figure 3.5: Optical conductivity spectra at various temperatures in $La_{1-x}Sr_xMnO_3$; (a) $x = 0.1$, (b) $x = 0.175$, and (c) $x = 0.3$. The hatched curves represent the temperature-independent parts of the spectra deduced from the envelope of the respective curves.

$\sigma(\omega)$ spectrum. In Fig. 3.6(a), (b), and (c), we show $\tilde{\sigma}(\omega)$ spectra for $x = 0.1, 0.175$, and 0.3, respectively.

We omitted the infrared phonon parts to avoid complexity. In Fig. 3.6(a) ($x = 0.1$), the spectral weight in the mid-infrared region increases with decrease of the temperature. On the other hand, Fig.3.6(b) and (c) ($x = 0.175$ and 0.3) show that the gap-like transition on the higher energy side above T_c is gradually reduced in intensity and changes into the $\omega = 0$ centered band as temperature decreases.

The formation of a mid-infrared peak as observed in the low-temperature $\tilde{\sigma}(\omega)$ spectra for $x = 0.1$ is often seen in the spectra of low-doped Mott-insulators which still remain insulating or semiconducting due to some localization effect [43, 41, 44, 45]. In general, such a mid-infrared peak eventually shifts to lower energy forming an $\omega = 0$ centered peak (a quasi-Drude band) upon the insulator-metal transition with further doping. The observed change of the ground state $\tilde{\sigma}(\omega)$ spectra in going from $x = 0.1$ to $x = 0.175$ (see and compare the 9 K $\tilde{\sigma}(\omega)$ spectra shown in Fig. 3.6) is consistent with this general tendency. The localization of doped carriers in the $x = 0.1$ manganite is likely to come from the Jahn-Teller (JT) type electron-lattice coupling (formation of JT polarons) [48, 49] in addition to the conventional random potential effect due to the alloying of the (La,Sr)-site. In this case, the spin-polarized e_g conduction bands are subject to the splitting (Δ_{JT}) due to the JT distortion, as schematically shown in Fig. 3.7(b), as well as in the paramagnetic case (Fig. 3.7(a)). Then the lower-lying $\tilde{\sigma}(\omega)$ band has a character of the interband transitions between the JT-split up-spin bands. The growth of the spin-polarization with decrease of temperature should tend to increase the spectral intensity because of the effective increase in the e_g electron transfer interaction. The feature is in accord with the observed result and also clearly demonstrated by the dynamical mean-field calculation for the strong JT-coupling case by Millis *et al.* [48] who have taken into account the both double-exchange and JT interactions as shown in Fig. 3.8. The band peak energy (≈ 0.5 eV) observed in the $x = 0.1$ spectra thus gives a measure of the binding energy (Δ_{JT}) of the JT polaron.

The spin-polarization dependent change in $\tilde{\sigma}(\omega)$ for the ferromagnetic metallic phase ($x = 0.175$ and $x = 0.3$) may be interpreted more straightforwardly in terms of the simple

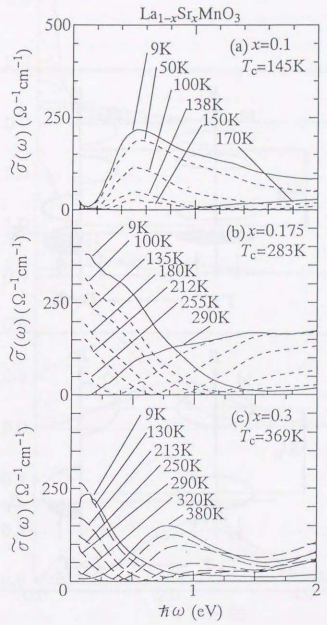

Figure 3.6: Reduced optical conductivity spectra which are derived by subtracting the temperature independent part (the hatched curves in Fig. 5) at various temperatures in $La_{1-x}Sr_xMnO_3$; (a) $x = 0.1$, (b) $x = 0.175$, and (c) $x = 0.3$. The far-infrared region dominated by the optical phonons is omitted to avoid complexity.

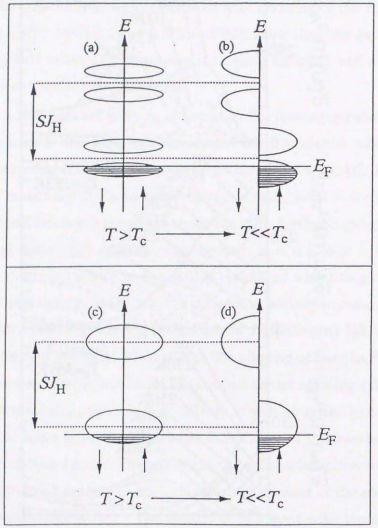

Figure 3.7: Schematics for the variation of the spin-polarized conduction e_g bands with temperature in the double-exchange manganites in the presence (upper panel (a) and (b)) and absence (lower panel (c) and (d)) of Jahn-Teller distortions.

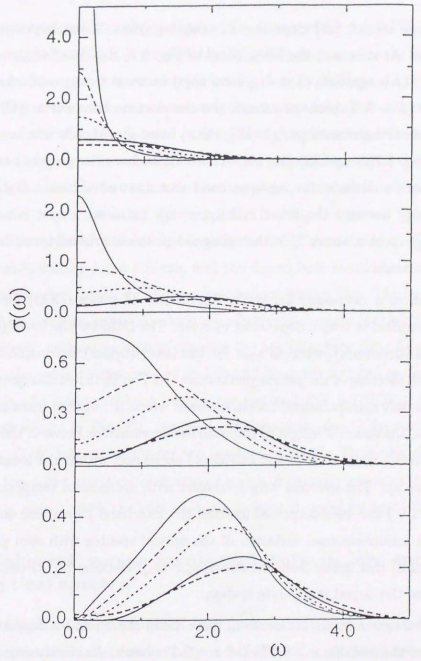

Figure 3.8: The temperature dependence of $\sigma(\omega)$ calculated by considering the dynamical Jahn-Teller distortions (From Ref. [48]). The lowest panel shows the spectra in the strong coupling case. As the temperature decreases from T_c (i.e., from a bald line to a simple line via dotted lines) the spectral weight around lower energy is accumulated.

double-exchange model, [28] since the JT coupling effect is less important for higher-x metallic phase. As shown in the lower panel of Fig. 3.7, the Hund's-rule coupling energy SJ_H (S being the magnitude of the t_{2g} local spin) between the e_g conduction carriers and t_{2g} local spins ($S = 3/2$) perhaps exceeds the one-electron bandwidth (W) of e_g electrons [27]. Under this circumstance ($SJ_H > W$), the e_g band should split into two bands by SJ_H as shown in Fig. 3.7(c) and (d) [28, 29]. Above T_c, such exchange-split bands are equally composed of two subbands, i.e., up-spin band and down-spin band. Optical transitions are allowed only between the lower and upper up- (or down-) spin bands. A gap-like feature in $\tilde{\sigma}(\omega)$ spectra above T_c is thus assigned to the interband transition between the exchange-split bands.

As temperature is decreased below T_c, the density of states (DOS) for the respective subbands is modified in a spin dependent manner: The DOS for the lower (upper) up-spin band increases (decreases), whereas that for the lower (upper) down-spin band decreases (increases) with increase of the net magnetization. At $T = 0$, the exchange-split bands turn into two completely spin-polarized bands, between which the optical transitions are forbidden. Therefore, the spectral weight of the *interband* transitions between the exchange-split bands is decreased, while that of the *intraband* excitation within the lower up-spin band gradually grows up. The spectral weight transfer with decrease of temperature as seen in Fig. 3.6(b) and (c) can be interpreted as from the interband transitions to the intraband ones. Such an unconventional variation of the optical spectra with spin polarization (or with temperature) thus arises from the strong spin (t_{2g})-electron (e_g) coupling ($SJ_H > W$) characteristic of the doped manganite system.

Keeping the above in mind, let us see in more detail the T- and x-dependent changes in $\tilde{\sigma}(\omega)$ spectra for the metallic $x = 0.175$ and $x = 0.3$ crystals. As clearly seen in Fig. 3.6, the energy scale of the spectral weight transfer is decreasing with hole doping. The peak energy of the upper exchange-split band in $\tilde{\sigma}(\omega)$ should approximately correspond to SJ_H (in the definition of J_H by eq. (1)) [29]. For $x = 0.175$, $SJ_H \approx 2$ eV, which is consistent with the estimate based on the optical spectrum of $LaMnO_3$ [38]. But the effective value of SJ_H is estimated as ≈ 0.9 eV for $x = 0.3$ by taking the peak position of the interband transitions in the $\tilde{\sigma}(\omega)$ spectrum, and is considerably smaller than that for $x = 0.175$. This means that spin-charge coupling strength as measured by SJ_H/W is decreased as the hole concentration x is increased. The present spectroscopic results directly indicate the crossover from the strong coupling to the medium or weak coupling regime with hole-doping. The origin of the variation of the effective J_H-value with x may be explained as follows: We have so far assumed that the spin-polarized conduction bands are of $3d$ e_g orbital character. However, this picture is too simple for a quantitative argument of the electronic structure and the p-hole character has to be taken into account. In fact, the parent compound $LaMnO_3$ should rather be sorted into the charge-transfer insulator than the Mott-Hubbard insulator in the Zaanen-Sawatzky-Allen scheme, and the doped hole should be in the strongly d-p hybridized state as evidenced by photoemission spectroscopy [24]. The larger admixture of the p-hole character then tends to reduce the effective exchange-splitting, since the effective antiferromagnetic exchange coupling between the Mn local spin ($S = 2$) and p-hole spin is mediated by the second order process and should be much reduced as compared with the bare J_H-value. As evidenced by a fairly large (by ≈ 1 eV) red shift of the 4 eV charge-transfer band shown in Fig. 3.3, the Sr-doping up-shifts the O $2p$ state in general and increases the O $2p$ hole character for the conduction band. Thus, the effective exchange splitting of the spin-polarized conduction band is nominally screened and reduced with hole-doping x, even though the bare J_H-value is least changed by hole-doping.

3.3.2 Coherent versus incoherent part in low energy part of optical spectra

We show in Fig. 3.9 a magnification of $\sigma(\omega)$ for $x = 0.175$ in the low-energy region. With decrease of temperature, the conductivity at 0.05–0.1 eV is increased nearly independently of photon energy. By contrast, the 9K spectrum below 0.05 eV steeply increases with decrease of photon energy indicating presense of a Drude peak characteristic of the metallic state. The value of dc conductivity $\sigma(0)$ at 9 K is 2.6×10^3 $\Omega^{-1}\text{cm}^{-1}$ (see Fig. 3.1), and comparable to that obtained by extrapolating the $\sigma(\omega)$ spectrum.

Such a Drude part is observed notably as well in the $\sigma(\omega)$ spectra of $x = 0.3$, as shown

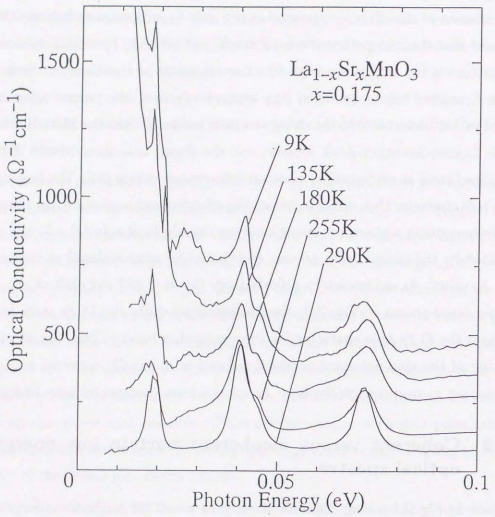

Figure 3.9: Low-energy parts of optical conductivity spectra in $La_{1-x}Sr_xMnO_3$ ($x = 0.175$) at various temperatures.

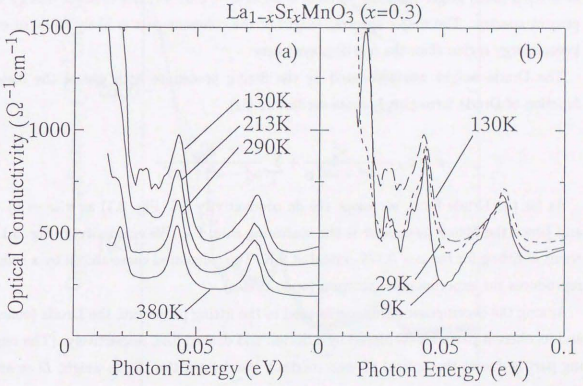

Figure 3.10: Low-energy parts of optical conductivity spectra in $La_{1-x}Sr_xMnO_3$ ($x = 0.3$) at 130–380 K (a) and at 9–130 K (b).

in Fig. 3.10(a) and (b). As temperature is decreased, the conductivity is at first increased below 0.1 eV from 380 K to 130 K (see Fig. 3.10(a)), but rather decreased when temperature is further lowered below 130 K (see Fig. 3.10(b)). The observed spectral change reminds us of the infrared feature of the c-axis spectra of the cuprate superconductors in which $\sigma(\omega)$ is supressed with decrease of temperature giving rise to a δ -function peak below T_c [50]. The value of the dc conductivity from the resistivity measurements ($\sigma(0) \approx 10^4\ \Omega^{-1}\mathrm{cm}^{-1}$ at 9 K) is much larger than the value of $\sigma(\omega)$ at $\omega = 0.01$ eV, the smallest energy in the present spectra. The major spectral weight of the coherent part is likely to lie in even a lower-energy region than the one displayed here.

The Drude weight was estimated by the fitting procedure with use of the dielectric function of Drude form plus Lorentz oscillators [51],

$$\tilde{\varepsilon} = \varepsilon_\infty - \frac{\omega_p^2}{\omega^2 + i\omega\Gamma_D} + \sum_j \frac{S_j}{\omega_j^2 - \omega^2 + i\omega\Gamma_j} \quad . \tag{3.1}$$

As for the Drude form, we adopt the dc conductivity (cf. Fig. 3.1) as $\sigma(\omega \to 0)$ value and hence the fitting parameter is the scattering rate, Γ_D. We exemplify in Fig. 3.11 the result of fitting for the $x = 0.175$ crystal at 9 K. The calculated curve shown by a solid line reproduces the experimental spectrum (open circles).

Among the decomposed components used in the fitting procedure, the Drude (coherent) and incoherent parts are displayed by a dotted and dashed line, respectively. (The remaining part is due to the optical phonon modes.) We defined the Drude weight D as area of the Drude part.

We may deduce the spectral weight of the inner-gap absorption, i.e., summation of the coherent (Drude) and incoherent parts, which is defined by the following relation:

$$\tilde{N}_{\mathrm{eff}}(\omega_c) = \frac{2m}{\pi e^2 N} \int_0^{\omega_c} \tilde{\sigma}(\omega) d\omega. \tag{3.2}$$

Here, N represents the number of formula units (i.e., the number of Mn atoms) per unit volume. For the cutoff energy $\hbar\omega_c$, we choose the energy at which the reduced optical conductivity $\tilde{\sigma}(\omega)$ shows a well-defined minimum making a distinction between the interband

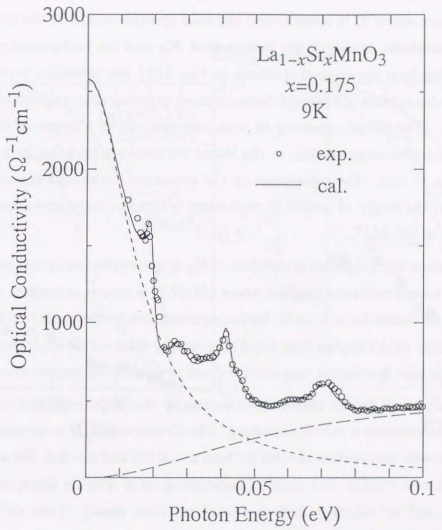

Figure 3.11: The parameter-fitted result (a solid line) of optical conductivity spectrum at 9 K (open circles) in $La_{1-x}Sr_xMnO_3$ ($x = 0.175$) using the Drude-Lorentz model (see text). The calculated Drude and incoherent part are shown by a dotted and dashed line, respectively.

and intraband excitations (see Fig. 3.6). We show in Fig. 3.12(a) and (b), the temperature dependence of the two parameters D (closed circle) and $\tilde{N}_{\rm eff}$ (open circle) in $x = 0.175$ (a) and $x = 0.3$ (b), respectively. [Note that $\tilde{N}_{\rm eff}$ for $x = 0.3$ excludes the T-independent contribution because of the aforementioned subtraction procedure. For $x = 0.3$, the paramagnetic phase above T_c is metallic and the total spectral weight of the incoherent part should be considered as sum of the T-dependent $\tilde{N}_{\rm eff}$ and the background part (perhaps ≤ 0.03 judging from the original spectrum in Fig. 3.5).] For reference, we also show the temperature dependence of square of the normalized ferromagnetic magnetization $(M/M_s)^2$ in the figure. (The measurements of M were performed under a magnetic field of 0.5 T.) M_s is the saturated magnetization at the lowest temperature ($\approx 4.0\mu_B$ in $x = 0.175$ and $\approx 3.5\mu_B$ in $x = 0.3$). The calculation by the dynamical mean-field approximation [29] indicates that the weight of intraband excitations within the lower exchange-split band is proportional to $(M/M_s)^2$.

As clearly seen, the temperature variation of $\tilde{N}_{\rm eff}$ is quite different from that of $(M/M_s)^2$: Even in the lower-temperature region where $(M/M_s)^2$ is almost saturated, $\tilde{N}_{\rm eff}$ keeps on changing, in particular for $x = 0.175$. Such a contradiction to the prediction by the simple double-exchange model implies that some large-energy scale carrier-scattering mechanism other than the spin fluctuation may survive down to much lower temperatures than T_c.

Anomalously small Drude weight as estimated by the aforementioned procedure may also be relevant to such a carrier-scattering. The Drude weight D is as small as ≈ 0.012 even for the lowest temperature spectra for both $x = 0.175$ and $x = 0.3$. For $x = 0.175$, the Drude weight is $\approx 1/5\tilde{N}_{\rm eff}$. In a simple Drude model, $D \propto n/m^*$, n being carrier number per Mn site, and m^* effective mass in unit of m_0 (bare mass). Then m^* is estimated to be ≈ 80, provided that the effective carrier density $n \approx 1$ as given by measurement of (ordinary) Hall coefficient [52]. However, such an enormously heavy mass as derived by this simplified interpretation appears to be incompatible with the results of electronic specific heat measurements by Kumagai *et al.* [53]: The conventional low-temperature T-linear specific heat is observed for the metallic phase ($x \geq 0.17$) and the coefficient γ is 5–6mJ/mol K^2, being nearly independent of x. The value is typical of the least-renormalized

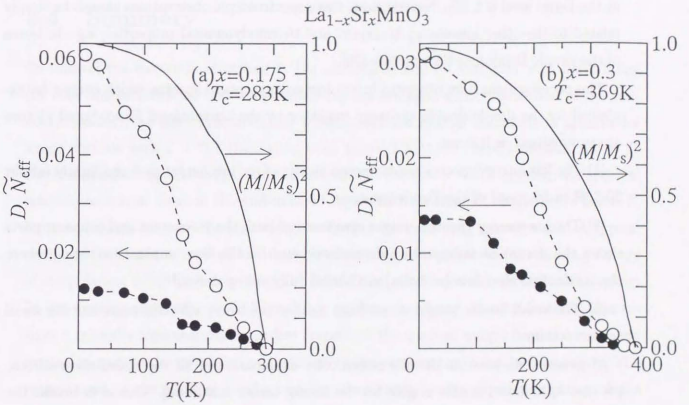

Figure 3.12: Temperature dependence of the inner-gap absorption $\tilde{N}_{\rm eff}$ (open circles) and Drude weight D (closed circles) in $La_{1-x}Sr_xMnO_3$ for $x = 0.175$ (a) and $x = 0.3$ (b) (see text). Broken lines are merely a guide to the eyes. The solid line shows the temperature dependence of square of the normalized ferromagnetic magnetization $(M/M_s)^2$, M_s being the saturated magnetization ($4.0\mu_B$ for $x = 0.175$ and $3.5\mu_B$ for $x = 0.3$) at the lowest temperature.

band mass $(2 - 3m_0)$. The behavior is also contrasted by the critically x-dependent mass renormalization as observed in the case of doped Mott insulators, such as $La_{1-x}Sr_xTiO_3$ [54]. It is worth noting here that the apparently very small Drude weight against the dominant incoherent-part is quite consistent with the valence-electron photoemission spectra of the relevant manganites in which the unconventionally small spectral weight is barely observed at the Fermi level [24, 55]. Nevertheless, these spectroscopic observations cannot be simply related to the other low-energy transport and thermodynamical properties, e.g., in terms of the simple Brinkman-Rice picture [56].

The peculiar behaviors observed in the low-energy optical spectra which cannot be explained by the simple double-exchange model or by the conventional Fermi-liquid picture are summerized as follows;

(1) The low-energy spectra are composed mostly of the incoherent part and lightly (about 20-30% in fraction) of the Drude response.

(2) The low-energy spectral weight composed of both the incoherent and coherent parts shows the persistent temperature dependence even in the low-temperature region where the conduction electrons (or holes) are almost fully spin-polarized.

(3) The small Drude weight arises from neither the heavy effective mass nor the small carrier density.

At present, we have no definite scenario for explanation of all the above observations, yet may speculate possible origins for the strong carrier scattering. One is to invoke the dynamical Jahn-Teller effect. The persistent Jahn-Teller distortion may result in the formation of small polarons which are barely mobile even at low temperature. The minimal Drude weight, the dominant incoherent part, and their persistent temperature-dependence might be explained by this hypothesis, but the seemingly unrenormalized γ might hardly be reconciled. Another possible mechanism may be related to the orbital degree of freedom in the e_g conduction state. The orbital may show the strong correlation and fluctuation even in the almost fully spin-polarized state. As an origin of the anomalous metallic state of $La_{1-x}Sr_xMnO_3$ as observed here, Ishihara, Yamanaka, and Nagaosa [57] have recently proposed the concept of the orbital liquid in which the 'ferromagnetic' correlation of the

$d_{x^2-y^2}$ orbitals and the resultant two-dimensional electronic character is enhanced but can be disordered down to low temperature. The internal consistency and discrepancy among the results of various measurements should be further investigated to unravel the nature of this intriguing novel metallic state.

3.4 Summary

To unravel the electronic structure in $La_{1-x}Sr_xMnO_3$ and its variation with band filling (or hole concentration x) and temperature (or the averaged spin-polarization of the conduction holes), we have systematically investigated the optical conductivity spectra for single crystals with $x = 0.1$ (insulating even below T_c), 0.175 (barely metallic below T_c but semiconducting above T_c), and 0.3 (metallic). For the $x = 0.1$ crystal, the spectral intensity is accumulated in the mid-infrared region with decrease of temperature below T_c but never comes close to the zero-energy reflecting the insulating ground state. A typical energy (0.5 eV) of the mid-infrared band is considered as representing the binding energy of the polarons which may arise from the Jahn-Teller or relevant electron-orbital coupling. In the metallic crystals, $x = 0.175$ and 0.3, on the other hand, the conductivity spectra show a critically temperature-dependent transfer of the spectral weight from the interband excitation part to the intraband one relating to the exchange-split conduction bands. The energy scale of the spectral weight transfer corresponds to the effective splitting of the spin-polarized conduction band due to the large Hund's-rule coupling energy exceeding the bandwidth; approximately 2 eV for $x = 0.175$ and 0.9 eV for $x = 0.3$. The observed x-dependent change of the band splitting energy is perhaps ascribed to the increasing p-hole character with x.

The intraband transitions in the metallic phase, which dominate the spectrum up to ≈ 1 eV, is far from the conventional Drude spectrum but should mostly be considered as an incoherent part. In fact, the real Drude part is discernible below 0.04 eV but with anomalously small spectral weight (roughly 1/5 of the total intraband spectral weight). The spectral weight of the incoherent plus coherent parts grows with the spin-polarization as expected

from the exchange-split band feature. However, the spectral weight keeps on changing in a sufficiently low temperature region (say below 50K) in which the spin-polarization (or ferromagnetic magnetization) nearly saturates. These features may indicate the presence of the strong carrier scattering process other than the spin-fluctuation being persistent down to low temperature. Such a strong carrier scattering mechanism may also be responsible for the squeezed Drude weight. This is inherently not included in the simple double exchange model and perhaps relevant to the orbital degree of freedom of the e_g spin-polarized electrons (or holes) or to the resultant dynamical Jahn-Teller coupling. The anomalously small Drude weight is simply related neither to heavy carrier mass nor to small carrier density, since the opposite situation has been observed in measurements of electronic specific heat and Hall coefficient. The dynamics of the fully spin-polarized electrons (or holes) with retaining orbital degrees of freedom in the doped perovskite manganites thus gives rise to unconventional metallic phase, the origin of which deserves for a further study.

Chapter 4

Charge ordering and disordering transitions in $Pr_{1-x}Ca_xMnO_3$ ($x = 0.4$) as investigated by optical spectroscopy

4.1 Introduction

In this chapter, we discuss temperature and magnetic field dependence of optical spectra in the colossal magnetoresistive manganite, $Pr_{1-x}Ca_xMnO_3$ $x = 0.4$. First, let us make a brief introduction again about the phase diagram of the charge ordering/disordering transitions and clarify routes we had adopted within the electronic phase diagram in the optical measurements. Figure 4.1(a) shows the phase diagram in the temperature and magnetic field plane for $Pr_{1-x}Ca_xMnO_3$ ($x = 0.4$) [17]. This compound undergoes the charge/orbital-ordering transition at $T_{co} \approx 235$K under zero field, and the nominal Mn^{3+} and Mn^{4+} species are regularly arranged below T_{co} as shown in the Fig. 4.1(b). Upon the charge ordering, $d_{3x^2-r^2}$ and $d_{3y^2-r^2}$ orbitals at Mn^{3+} site are alternatively ordered in the *ab*-plane [30], as also shown in Fig. 4.1(b). As the temperature is decreased, antiferromagnetic spin ordering subsequently occurs ($T_N \approx 170$ K, a closed triangle in Fig. 4.1(a)). The pattern of spin ordering below T_N is so called *CE*-type [30, 31]. (To be precise on the basis of the neutron diffraction measurement [30], the direction of the spin is canted from

the c-axis by $20-30$ degree.) With the decrease of temperature below T_N, the canted antiferromagnetic ordering occurs at $T_{CA} \approx 40$K (an open triangle in Fig. 4.1(b)). This order is perhaps a consequence of incommensurate hole-doping level ($x < 1/2$) and in the $x = 1/2$ crystal such a canted magnetic order has not been observed [31]. Under the external magnetic field, the CO state is transformed into a ferromagnetic metallic state as mentioned before. The hatched region in the Fig. 3.1(a) shows a field-hysteresis characteristic of the first-order phase transition. For example, the insulator-metal transition (IMT) is observed at 6.4 T and 4.2 T in the field-increasing and decreasing run, respectively. Hereafter, we show variation of the optical spectra along the two routes in the $H-T$ plane, which both cause the charge ordering/disordering transition, as shown in the upper panel of Fig. 4.1; (1) zero-field cooling (ZFC) run and (2) field-increasing and decreasing at a constant temperature, 30 K.

4.2 Temperature dependence of optical spectra

Figure 4.2 shows optical conductivity spectrum ($\sigma(\omega)$) in $Pr_{1-x}Ca_xMnO_3$ ($x = 0.4$) for $\mathbf{E}\|b$ and $\mathbf{E}\|c$ at 10 K. (Spiky structures below 0.06 eV are due to optical phonon modes.) In the CO state at 10 K (viewed as the graound state), the difference between the b- and c-axis polarized $\sigma(\omega)$ becomes large reflecting the anisotropy of the ordering pattern of the charge, spin, and orbitals (see Fig. 4.1(b)). The most notable anisotropic feature is that each $\sigma(\omega)$ has a different onset energy (Δ). To be more quantitative, we have estimated each Δ (Δ_b and Δ_c) by extrapolating linearly the rising part of the b- and c-axis polarized $\sigma(\omega)$ to the abscissa as shown by dashed lines in Fig. 4.2(b). It is reasonable to consider that the Δ_b is dominated by the optical transition of $d_{3x^2-r^2}$ (or $d_{3y^2-r^2}$) electron to the neighboring Mn^{4+} site with a parallel spin (see Fig. 4.1(b)). The $d_{3x^2-r^2}$ ($d_{3y^2-r^2}$) electron can hardly hop along the c-axis due to a small transfer integral as well as to a large on-site coulomb energy. The excess electrons which are introduced into the CE-type CO state by decreasing from x=1/2 are likely to occupy the $d_{3z^2-r^2}$ orbital of the Mn^{4+} site [30], so that the Δ_c originates from the intersite transition of such excess $d_{3z^2-r^2}$ electrons. The fact of

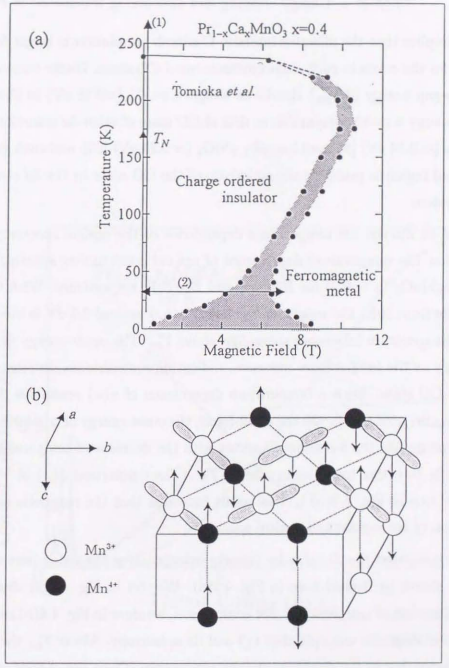

Figure 4.1: (a): The temperature and magnetic phase diagram of $Pr_{1-x}Ca_xMnO_3$ ($x = 0.4$) derived from ref [7]. The hatched area shows a field-hysteresis region. A closed triangle denotes the Neel temperature T_N, and an open one the canted antiferromagnetic transition temperature T_{CA}. (b): collinear CE-type spin and charge ordering structure. The hatched lobes show the orientation of $d_{3x^2-r^2}$ and $d_{3y^2-r^2}$ orbitals. (see text)

$\Delta_c < \Delta_b$ implies that the effective intersite Coulomb correlation is larger for the in-plane than that for the c-axis in such a discommensurated CO state. Under these circumstances, the charge-gap energy ($2\Delta_{gap}$) should be assigned to Δ_c ($\approx$0.18 eV) in the ground state. This gap-energy is quite comparable to that of CO state of other $3d$ transtion metal oxides, *e.g.*, Fe_3O_4 (≈ 0.14 eV) [55] and $La_{5/3}Sr_{1/3}NiO_4$ (≈ 0.24 eV) [63], and such gap-value in the mid-infrared region is probably characteristic of the CO state in the $3d$ strong correlated electron system.

Next, let us discuss the temperature dependence of the optical spectra. Figure 4.3(a) and (b) show the temperature dependence of optical conductivity spectra (10 K–293 K) in $Pr_{1-x}Ca_xMnO_3$ ($x = 0.4$) for $\mathbf{E}\|b$[(a)] and $\mathbf{E}\|c$[(b)], respectively. With the increase of temperature from 10K, the weight of b-polarized $\sigma(\omega)$ around 0.2 eV is increased and the shape of the spectrum becomes gapless-like above T_{co}. The onset energy of $\sigma(\omega)$ shifts to lower energy as the temperature increases, indicating a continuous decrease of the optical gap in the CO state. Such a temperature dependence of $\sigma(\omega)$ resembles that of the CO system, $La_{5/3}Sr_{1/3}NiO_4$ [63]. On the other hand, the onset energy of c-polarized $\sigma(\omega)$ moves to higher energy like the b-polarized spectra with the decrease of temperature from T_{co} to T_N, but shifts to rather lower energy below T_N. (The c-polarized $\sigma(\omega)$ at 10K was drawn with a bold line in Fig. 4.3(b).) This result indicates that the magnetic ordering affects the evolution of the c-polarized optical spectra.

We have estimated the Δ-value by linearly extrapolating the rising-part of $\sigma(\omega)$ to the abscissa as shown by dashed lines in Fig. 4.2(a). We plot in Fig. 4.4(a) thus obtained Δ-values as a function of temperature. For comparison, we show in Fig. 4.4(b) the temperature dependence of magnetic susceptibility (χ) and its anisotropy. Above T_{co}, the magnitude of χ is fairly large due to the double-exchange mechanism. Once the charge-ordering occurs ($T < T_{co}$), however, the χ-value is abruptly suppressed, because the double-exchange interaction is essentially quenched. While anisotropy of the magnetic susceptibility was scarcely observed in the paramagnetic state ($T > T_N$), there exists a clear anisotropic feature in the temperature region lower than T_N. The χ measured under $\mathbf{H}\|c$ is decreased with a cusp structure at T_N but under $\mathbf{H}\|b$ is almost constant below T_N, indicating that

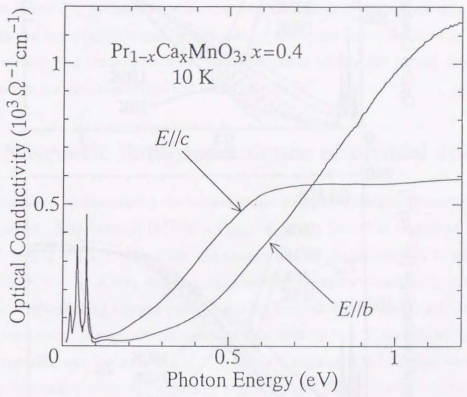

Figure 4.2: Optical conductivity spectra at the graound state of CO state (10 K).

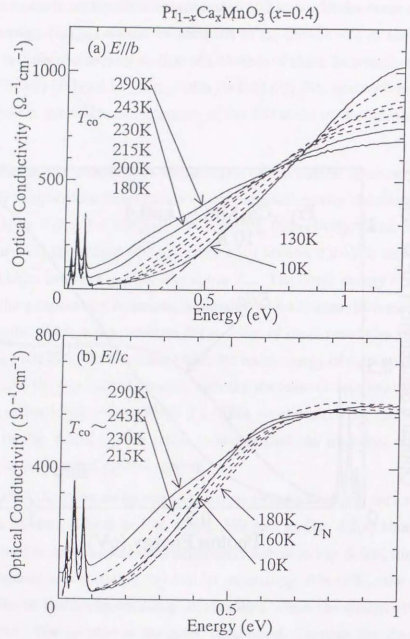

Figure 4.3: The temperature-variation of the optical conductivity spectra in a single crystal of $Pr_{1-x}Ca_xMnO_3$ ($x = 0.4$) for (a) E$\|b$ and (b) E$\|c$ polarization.

an easy axis of sublattice magnetization approximately directs the c-axis. (The increase in χ below $T \approx 100$K is due to the canted antiferromagnetic order [31].) These results are consistent with those of the neutron scattering measurements [30].

Keeping the above in mind, let us discuss the T-dependence of the anisotropic Δ-value (the Fig. 4.4(a)). In the whole temperature region below T_{co}, the Δ_c-values are always smaller than Δ_b. With decreasing temperature, Δ_b is monotonically increased and scarcely affected by the antiferromagnetic spin-ordering in ab-plane. By contrast, the Δ_c is rather decreased below T_N, perhaps because the c-axis hopping of the excess $d_{3z^2-r^2}$ carriers is favored by the ferromagnetic spin-ordering along the c-axis below T_N (see Fig. 4.1(b)). This may be viewed as a consequence of one-dimensional (along the c-axis) double-exchange interaction in the *electron-doped* CO state ($x < 0.5$).

4.3 Magnetic field dependence of optical spectra

The next issue to be discussed is the variation and collapse of the gap structure in the course of the magnetic field-induced IMT in a $Pr_{1-x}Ca_xMnO_3$ ($x = 0.4$) crystal at 30 K (see the route (2) in Fig. 4.1(a)). We show the magnetic field dependence of b- and c-polarized $R(\omega)$ at 30 K in Fig. 4.5(a) and (b), respectively. A spiky structure around 0.06 eV is due to the highest-lying oxygen phonon mode. In both the b- and c-polarized $R(\omega)$, the infrared reflectivity is gradually increased with a field up to 6 T, and abruptly transformed into the metallic one between 6 and 7 T. Such a huge spectral change with an external magnetic field over a wide photon energy region up to 3 eV (as it were *magnetochromism*) has seldom been observed so far. We show the b- and c-polarized $\sigma(\omega)$ spectra deduced by K-K analysis in Fig. 4.6(a) and (b), respectively. With increasing of magnetic field, the onset of $\sigma(\omega)$ gradually shifts to lower energy, and at 7 T the $\sigma(\omega)$ undergoes a large change into a metallic band, as expected from the variation of $R(\omega)$. We estimated Δ by means of the same extrapolating procedure as in the analysis of ZFC spectra.

We show in Fig. 4.7(a) a variation of Δ-value with a magnetic field at 30 K both for the field-increasing and decreasing runs.

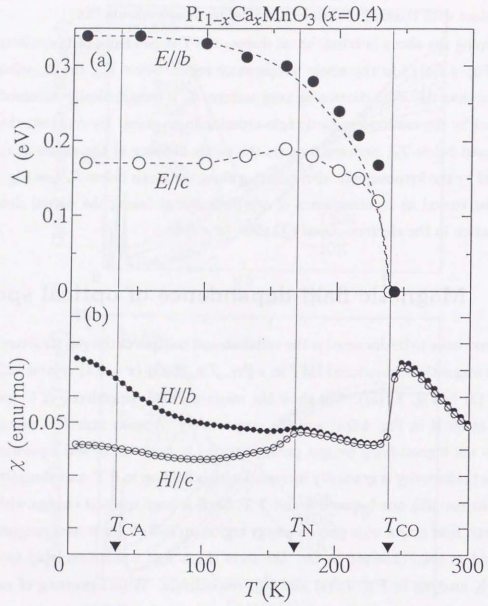

Figure 4.4: (a): The temperature dependence of energies of polarized gap transition, Δ_b (closed circle) Δ_c (open one), in $Pr_{1-x}Ca_xMnO_3$ ($x = 0.4$). (b): The temperature dependence of the magnetic susceptibility χ and its anisotropy.

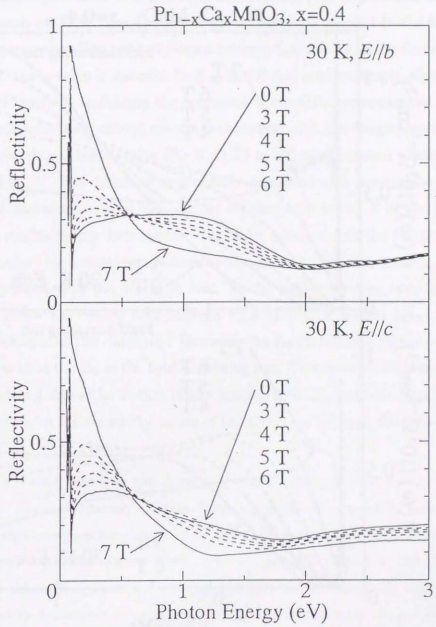

Figure 4.5: (a) [(b)]: The magnetic field dependence of b [c]-polarized reflectivity spectra of $Pr_{1-x}Ca_xMnO_3$ ($x = 0.4$) at 30 K.

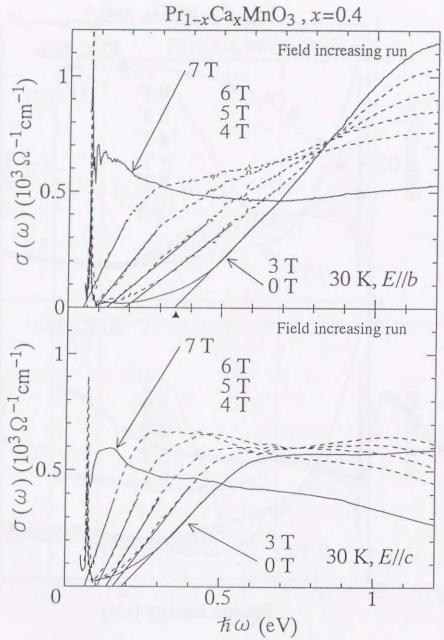

Figure 4.6: (a) [(b)]: The magnetic field dependence of b [c]-polarized optical conductivity spectra at 30 K deduced by Kramers-Kronig analysis.

For comparison, we show in Fig. 4.7(b) the magnetic field dependence of resistivity (ρ) along the b-axis at 30 K. The applied magnetic field was parallel to the b-axis as in the optical measurements. The ρ steeply drops between 5 and 6.5 T in the field-increasing run. Above 6.5 T the ρ-value is metallic ($\approx 5 \times 10^{-4}\Omega$ cm) and no longer affected by further increasing of the field, indicating the occurence of the fully spin-polarized metallic state. The observed variation of optical spectra is consistent with this magnetoresistive behavior. As mentioned above, the Δ-value (30 K, 0 T) is different between along the b- and c-axis by ≈ 0.18 eV. The difference is gradually decreased with a magnetic field and both the Δ_b- and Δ_c-values become zero almost continuously at 6.5 T in the field-increasing run. These results clearly indicate that the order parameter of the CO state, which can hardly be probed by resistivity measurements, continuously decreases and the anisotropy of Δ is suppressed with the magnetic field. In the field-decreasing run, the gap-opening is observed below the critical field between 4.5 and 4 T, in accord again with the field-hysteretic behavior of the resistivity. However, the Δ_b and Δ_c are rather comparable and obviously less than the Δ_b in the field-increasing run. This irreversible behavior is perhaps due to the strong first-order nature of the present field-induced transiton, but consistent with a difference in the resistivity values of the CO state between the field-increasing and decreasing runs.

It is worth noting here that the Δ-value gradually changes with a magnetic field while the $\sigma(\omega)$ (or $R(\omega)$) drastically changes from a gap-like to a metallic feature around 6.5 T. Such a large energy-scale change upon the IMT is reminiscent of the Mott transition in the electron correlated system. As in a barely metallic state near the Mott transition, the spectral shape of $\sigma(\omega)$ at 7 T, where the metallic ferromagnetic state is realized, is only moderately dependent on ω, being far from a simple Drude shape. The value of the dc-conductivity ($\sigma(0)$) at 30 K and 7 T is $\approx 2 \times 10^3 \Omega^{-1}\mathrm{cm}^{-1}$ (see Fig. 4.7(b)) and merely about twice the value of $\sigma(\omega)$ at 0.06 eV. These results imply that the charge dynamics in the field induced metallic state is highly diffusive or incoherent [64], which is also consistent with the results of $La_{1-x}Sr_xMnO_3$ near the metal-insulator phase boundary [60].

This anomaly below T_N is due to the spin-ordering structure of modified CE-type;

namely, ferromagnetic along the c-axis but antiferromagnetic in the ab-plane. The x=0.4 compound shows the magnetic field-induced insulator to metal transition and we have investigated the electronic-structural change at 30 K with an external magnetic field. Both the b- and c-polarized spectra drastically change from an insulating low-reflectivity to a metallic high-reflectivity band at 6.5 T. The magnitude of Δ_b and Δ_c obtained from the respective $\sigma(\omega)$ gradually decrease with a magnetic field and disappears at 6.5 T. These results indicate the rather continuous change in the electronic structure from the anisotropic charge-ordered state to the isotropic ferromagnetic metal.

4.4 Summary

In summary, we have observed the variation of optical spectra and their anisotropy with magnetic field for a single crystal of $Pr_{1-x}Ca_xMnO_3$ ($x = 0.4$). In the ground state of the charge ordered (CO) state (10 K), Δ_c (the onset energy of c-polarized optical conductivity) is smaller than Δ_b, which is anticipated from the proposed spatial pattern of the charge and orbital ordering in the CO state. The optical gap energy at 10 K is estimated as ≈ 0.18 eV, which is comparable to other CO systems. As the temperature is decreased, Δ_b keeps on increasing while the Δ_c begins to rather decrease below T_N. This anomaly below T_N is due to the spin-ordering structure of modified CE-type; namely, ferromagnetic along the c-axis but antiferromagnetic in the ab-plane. We have investigated the electronic-structural change in the course of the magnetic field-induced insulator-metal transition at 30 K. Both the b- and c-polarized spectra drastically change from an insulating low-reflectivity to a metallic high-reflectivity band at 7 T over a wide photon energy region (0.05 eV–3 eV). The magnitude of Δ_b and Δ_c obtained from the respective $\sigma(\omega)$ gradually decrease with a magnetic field and disappears at 6.5 T. These results indicate the rather continuous change in the electronic structure from the anisotropic CO state to the isotropic ferromagnetic metal.

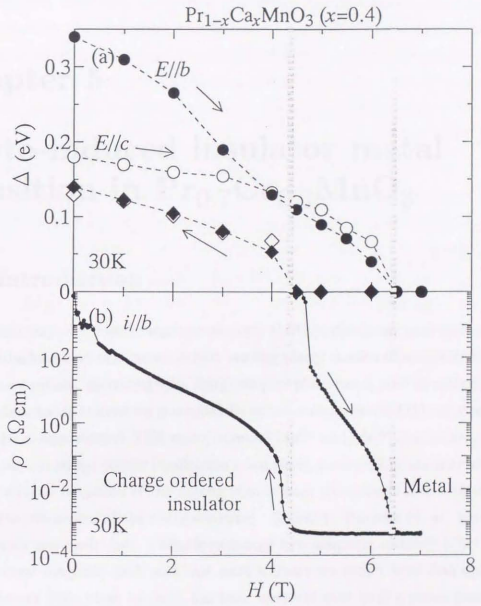

Figure 4.7: (a): The magnetic field dependence of the Δ_b (closed symbols) and Δ_b (open ones) in the field-increasing run (circles) and decreasing run (squares) for $Pr_{1-x}Ca_xMnO_3$ ($x = 0.4$). (b): The magnetic field dependence of resistivity (ρ).

Chapter 5

Photo-induced insulator metal transition in $Pr_{0.7}Ca_{0.3}MnO_3$

5.1 Introduction

Since a discovery of colossal magnetoresistance (MR) phenomena, perovskite-type manganese oxides have been of current interest. Among a large number of manganites, $Pr_{1-x}Ca_xMnO_3$ system shows various interesting spin-charge coupled phenomena, such as real space charge-ordering/disordering transitions controlled by an external magnetic field, as mentioned before. In the charge-ordered (CO) state, nominal Mn^{3+} and Mn^{4+} species are alternately arranged and the strong carrier localization takes place. Such a CO state is most stabilized at x=0.5 and the deviation of the doping level x from the commensurate value (x=1/2) weakens the robustness of the charge-ordering. Recently, Tomioka *et. al.* revealed that the CO state can 'melt' into a double-exchange ferromagnetic metallic (FM) state [15] under external magnetic field, and that such a phase transition is of first order with a large hysteresis [58]. More lately, it has been observed that such a phase transition can be triggered by other external stimuli than a magnetic field: Keimer and his coworkers found the insulator-metal (I-M) transition by illumination with X-ray in the x=0.3 crystal [32], and Asamitsu *et al.* observed that the conductivity in the same compound shows an abrupt increase with increase of electric field [59]. Another example is the I-M transition triggered by 'photocarrier injection' with visible-IR laser [33].

These results, which are interesting also in the light of the technical application, are summarized by schematic diagrams as shown in Fig. 5.1. Such phase transitions from the CO insulating state to the FM one are of first order with a large hysteresis. The energy levels of the two states are almost degenerate in the hysteresis region, which suggests that external stimuli (and their combination) can switch the electrical (I-M) as well as magnetic (antiferromagnetic-ferromagnetic) state. Thus, the $Pr_{1-x}Ca_xMnO_3$ system offers a versatile stage of 'phase control'.

Figure 5.2 shows time dependence of voltage drop caused by irradiation of a laser pulse at 30 K investigated by Miyano *et al.* [33]. The value of the voltage drop was measured across a 50 Ω load resister as depicted in the inset and the applied voltage 11 V is much smaller than the critical voltage at which the electric field-induced I-M transition takes place. The voltage drop rapidly increases up to ≈2 V just after the photo-excitation and such anomalous photocurrent once decays very slowly. However, the voltage drop across the sample gradually increases again after ≈ 30 μs, and is eventually stabilized around 7.8 V as indicated by an arrow. The final sample resistance is ≈5 Ω and much smaller than that before the photo-excitation (> 1 GΩ). These results clearly indicate that the I-M transition is realized by the photocarrier injection into the CO state. Such a highly conductive state returns to the insulating one when the applied voltage is removed. It is likely that the electric current sustains the metallic domains produced by the photocarrier injection, forming current paths against the back pressure from the insulating (CO) medium. In fact, the threshold laser power for the photo-induced phase transition was observed to be reduced with increase of the applied electric field. This result is very interesting, but the problem is that it is difficult to investigate the electronic properties of such photo-induced highly conductive state in detail because the applied field is indispensable to keep the FM state. In this chapter, we investigate the I-M transtion with photo-excitation under 1.2 T of magnetic field instead of the electric filed in $Pr_{1-x}Ca_xMnO_3$ (x=0.3) crystal, and discuss the electric and magnetic response of the photo-injected CO state.

Before the discussion of the photo-induced transition, we show in Fig. 5.3 the temperature dependence of resistance (R) under 1.2 T in the temperature increasing- and decreasing-run. Below $T_{co} \approx$ 200 K, the R in the x=0.3 compound shows insulating behavior in both the running. This result clearly indicates that the 1.2 tesla of magnetic field itself cannot realize the FM state at any temperature and a simple scenario such as laser-induced heating is excluded in this system. Hereafter, we discuss the nature of photo-induced I-M transition at 30 K under 1.2 T in the x=0.3 crystal.

5.2 Photo induced insulator metal transition

To be highlighted in this section is the I-M transition with photo-excitation in $Pr_{0.7}Ca_{0.3}MnO_3$. Figure 5.5(a) shows temporal variation of the resistance (R) after a pulsed photo-excitation under a magnetic field of 1.2 T. (No voltage was applied when the sample was shot with a laser pulse.) There is scarcely magnetoresistance effect under 1.2 T at any temperature in this compound, and the R-value at 30 K is very large (> 1 GΩ) before the photo-excitation. With a single laser shot, however, the R drastically decreases by more than nine orders of magnitude, indicating that the photo-induced I-M transition takes place. Such a large decrease of R continues until ≈100 s and it seems that the time scale of the decrease becomes more gradual after that. The latter slow variation of R is perhaps not directly relating to the photo-excitation, but is characteristic of the metastable state under the magnetic field, where the M shows gradual change as well (*vide infra*). The R-value finally decreases down to ≈ 103Ω after about five hours. Such a highly conductive state is preserved even after the magnetic field is removed. This is in contrast to the case of the photo-induced I-M transition under an electric field. We show in Fig. 5.5(b) temperature dependence of R (in the warming run) after photo-excitation under zero magnetic field. (The measurement was done during a much shorter period than the time scale of the gradual decrease of R.) The R-value shows an abrupt jump just below ≈70 K, which is consistent with the critical temperature for the magneto-transport measurements (see the inset of Fig. 5.3). This result clearly indicates that such a photo-induced conductive phase coincides with the FM state realized by a magnetic field. The large difference of the time scale of the photo induced I-M transition between under electric field (≈ μs, see Fig. 5.2) and under magnetic one

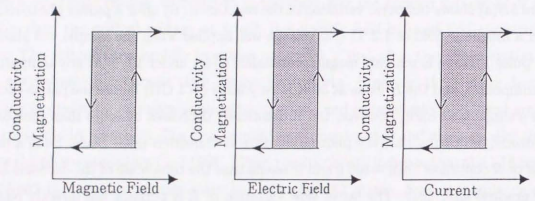

Figure 5.1: Exotic phase control achieved in $Pr_{1-x}Ca_xMnO_3$ system.

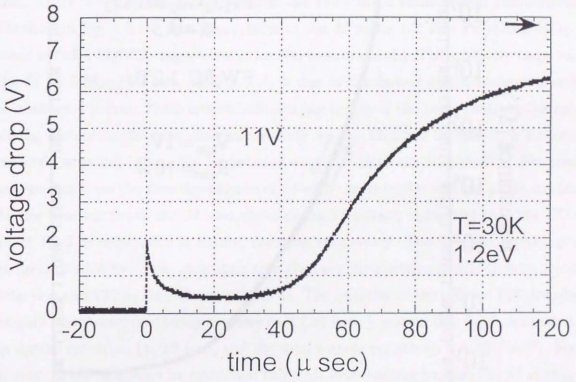

Figure 5.2: Time evolution of the resistance in $Pr_{1-x}Ca_xMnO_3$, $x = 0.3$ after a single shot of 1.2 eV laser pulse. An arrow denotes the value of the final voltage drop (from Ref. [33]).

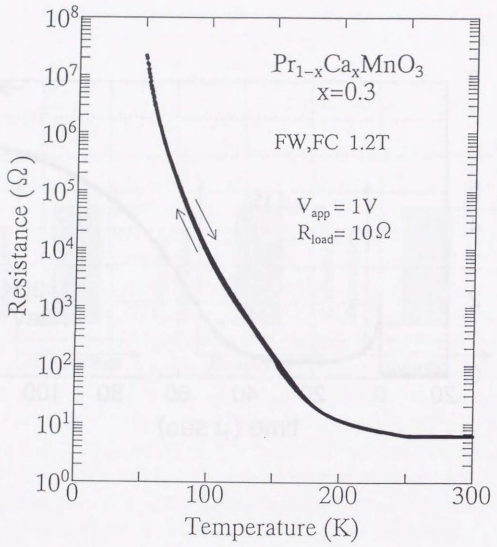

Figure 5.3: Temperature dependence of resistivity in $Pr_{0.7}Ca_{0.3}MnO_3$under 1.2 T. Inset shows the electronic phase diagram of the compound in the temperature vs. magnetic field plane.

(≈s, see Fig. 5.5) perhaps results from the different roles of these external fields during the photo-induced I-M transition: the electric field plays an important role in making current paths between FM domains as well as weakening the CO state, whereas the magnetic field only weakens the robustness of the charge-ordering. It is worth noting here that the time scale of the I-M transition with irradiation of X-ray (≈s) [32] is consistent with the latter case. There is a supporting evidence that the FM state is realized with photo-excitation. We show in Fig. 5.6 the time dependence of the M under 1.2 T in $Pr_{0.7}Ca_{0.3}MnO_3$. (We made use of a SQUID magnetometer for the measurement.) The relatively large value of the M ($\approx 0.88\mu_B$/Mn site, see Fig. 5.4) is due to the canted antiferromagnetic ordering as mentioned before. Three arrows indicates the timing of the pulse photo-excitation, and all the measurements were done successively for the identical sample with intermittent zero-field warming (up to 300 K) between events of the laesr illumination. For comparison, we also show the time dependence of M with closed circles without photo-irradiation. As the time increases, the M also shows gradual increase, indicating that the CO state under 1.2 T is metastable in nature, decaying very slowly. The M-value jumps upon the photo-excitation by $\approx 1\%$, indicating that the laser illumination clearly induces ferromagnetic domains ($3.5\mu_B$/Mn site, see Fig. 5.4). The quantity of the created FM domains are roughly reasonable considering the laser spot (≈1 mmϕ), penetration depth estimated from an optical spectrum (≈ 0.2 μm), and the total sample volume ($\approx 3 \times 10^{-4}$ cm^3). Such an increase of the M cannot be attributed to simple laser-heating because the M arising from the canted antiferromagnetic ordering would decrease upon heating. These results clearly indicate photo-induced fainal state is ferromagnetic.

5.3 Summary

We have studied the electronic-structural change from a charge ordered (CO) to a ferromagnetic metallic (FM) state with photo-excitation in $Pr_{1-x}Ca_xMnO_3$ (x=0.3). We have presented some evidences that the CO state can be transformed into the FM one with photo-excitation. Resistance drastically decreases with a single shot of visible/IR laser.

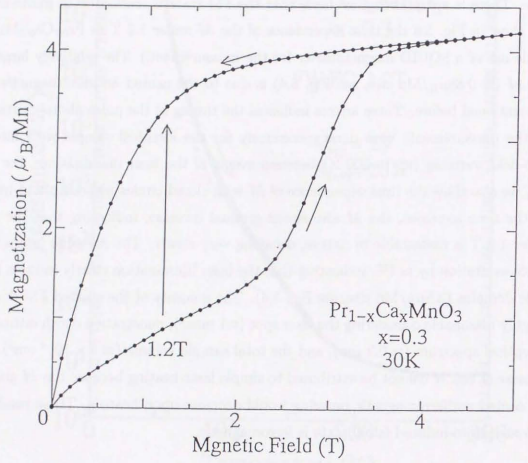

Figure 5.4: Magnetic field dependence of the magnetization in $Pr_{0.7}Ca_{0.3}MnO_3$at 30 K.

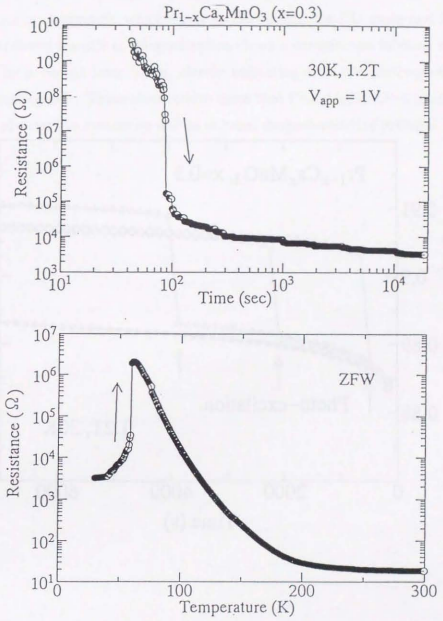

Figure 5.5: (a): Time evolution of the resistance in $Pr_{0.7}Ca_{0.3}MnO_3$under 1.2 T after photo-excitation. (b): The temperature dependence of the resistance in the zero-field warming-run.

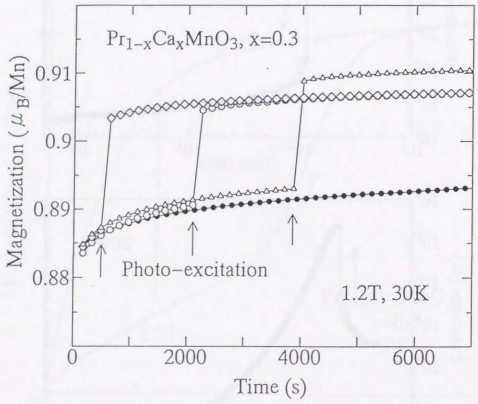

Figure 5.6: Evolution of magnetization by photo-excitation under 1.2 T and 30 K in $Pr_{0.7}Ca_{0.3}MnO_3$. Arrows show the timing of a pulse photo-excitation.

The time scale of such an insulator-metal transition depends on the type of the external field (electric or magnetic), which tends to destabilize the CO state and hence promote the photo-induced transition. Magnetization shows a conspicuous increase with the photo-excitation by a pulsed laser beam, clearly indicating that the photo-generated metallic state is ferromagnetic. These observations show that $Pr_{1-x}Ca_xMnO_3$ is promising as a new intriguing photoactive system as well as colossal magnetoresistive material.

Chapter 6

Conclusions

In this thesis, we have investigated optical properties of two types of the perovskite manganite: one is the conventional double-exchange ferromagnet, $La_{1-x}Sr_xMnO_3$, and the other the typical magnetoresistive manganite which shows charge-ordering/disordering phase transition, $Pr_{1-x}Ca_xMnO_3$system. The major results are listed as follows;

▷ We have investigated the optical spectra for single crystals with $x = 0.1$ (insulating even below T_c), 0.175 (barely metallic below T_c but semiconducting above T_c), and 0.3 (metallic) to unravel the electronic structure and its variation with band filling (x) and temperature.

• For the $x = 0.1$ compound, the spectral weight is increased in the mid-infrared region with decrease of temperature below T_c, and the typical energy (0.5 eV) of the mid-infrared band is considered as representing the binding energy of the polarons which may arise from the Jahn-Teller coupling.

• In the metallic crystals, $x = 0.175$ and 0.3, the conductivity spectra show a critically temperature-dependent transfer of the spectral weight from the interband excitation part to the intraband one relating to the exchange-split conduction bands over a wide photon energy region (approximately 2 eV for $x = 0.175$ and 0.9 eV for $x = 0.3$).

• The intraband transitions in the metallic phase, which dominate the spectrum up to ≈ 1 eV, is far from the conventional Drude spectrum but should mostly be considered as an highly diffussive or incoherent part and the real Drude part is discernible below 0.04 eV

but with anomalously small spectral weight, which cannot be elucidated in the light of the simple double exchange model or the dynamical Jahn-Teller coupling effect.

▷ We have observed the variation of optical spectra and their anisotropy with temperature and external magnetic field for a single crystal of $Pr_{0.6}Ca_{0.4}MnO_3$, which shows charge-ordering/disordering phase transtion.

• In the ground state of the charge ordered (CO) state (10 K), Δ_c (the onset energy of c-polarized optical conductivity) is smaller than Δ_b, which is expected from the proposed spatial pattern of the charge and orbital ordering in the CO state. The optical gap energy at 10 K is estimated as ≈ 0.18 eV, which is comparable to other CO systems.

• As the temperature is decreased, Δ_b keeps on increasing while the Δ_c begins to rather decrease below T_N. This anomaly below T_N is due to the spin-ordering structure of modified CE-type; namely, ferromagnetic along the c-axis but antiferromagnetic in the ab-plane.

• Both the b- and c-polarized spectra drastically change from an insulating low-reflectivity to a metallic high-reflectivity band at 7 T over a wide photon energy region (0.05 eV–3 eV).

• The magnitude of Δ_b and Δ_c gradually decrease with a magnetic field and disappears at 6.5 T. These results indicate the rather continuous change in the electronic structure from the anisotropic CO state to the isotropic ferromagnetic metal.

▷ In addition to the magnetospectroscopy in $Pr_{1-x}Ca_xMnO_3$, we have studied the electronic-structural change from a CO to a ferromagnetic metallic state with photo-excitation for the x=0.3 crystal. We have presented some evidences that the CO state can be transformed into the FM one with photo-excitation at 30 K and under 1.2 T of magnetic field.

• Resistance drastically decreases with a single shot of visible/IR laser.

• Magnetization shows a conspicuous increase with the photo-excitation by a pulsed laser beam, clearly indicating that the photo-generated metallic state is ferromagnetic.

Chapter 7

Acknowledgement

I wish to express my gratitude to Prof.Y. Tokura for his guidance, suggestion, discussion, and encouragement in the course of this work. I am grateful to Dr.Y. Tomioka, A. Urushibara, Dr.A. Asamitsu, and Dr.H. Kuwahara for synthesis of single crystals and their characterization. I also thank to Y. Onose and Y. Otsuka for their collaboration for optical measurements under magnetic field and resistance measurements with photo-excitation. I'm also grateful to Prof.T. Arima, H. Taniguchi, and T. Ishikawa for their technical assistance and encouragement in early stage of this work. I am indebted to Dr. T. Katsufuji for various kind of discussions and helpful comments. I'd like to thank to Dr.N. Furukawa and Dr.S. Ishihara for their theoretical suggestions and discussions. I am also grateful to Prof.H. Akiyama, Prof.A. Fujimori, Prof.M. Imada, Prof.H. Yoshizawa, Prof.S. Yamamoto, and Prof. K. Miyano for useful discussions. I thank all the members of Tokura laboratory and Tokura-group in *JRCAT*.

This work was supported in part by Grant-in-Aids for Scientific Research from the Ministry of Education, Science, Sport, and Culture, Japan, and by the New Energy and Industrial Technology Development Organization of Japan (NEDO).

Bibliography

[1] G. H. Jonker and J. H. van Santen, Physica **16**, 337 (1950).

[2] G. H. Jonker and J. H. van Santen, Physica **19**, 120 (1953).

[3] E. O. Wollan and W. C. Coehler, Phys. Rev. **100**, 545 (1955).

[4] C. Zener, Phys. Rev. **B 82**, 403 (1951).

[5] P. W. Anderson and H. Hasegawa, Phys. Rev. **100**, 675 (1955).

[6] P. -G. de Gennes, Phys. Rev. **118**, 141 (1960).

[7] R. M. Kusters, D. A. Singleton, R. McGreevy, and W. Heyes, Physica B **155**, 362 (1989).

[8] K. Chahara, T. Ohno, M. Kasai, and Y. Kozono, Appl. Phys. Let. **63**, 1990 (1993).

[9] R. von Helmolt, J. Wecker, B. Holzapfel, L. Schultz, and K. Samwer, Phys. Rev. Lett. **71**, 2331 (1993).

[10] Y. Tokura, A. Urushibara, Y. Moritomo, A. Asamitsu, G. Kido, and N. Furukawa, J. Phys. Soc. Jpn. **63**, 418 (1994).

[11] M. McCormack, S. Jin, T. H. Tiefel, R. M. Fleming, J. M. Phillips, and R. Ramesh, Appl. Phys. Lett. **64**, 3045 (1994).

[12] S. Jin, T. H. Tiefel, M. McCormack, R. A. Fastnacht, R. Ramesh, and L. H. Chen, Science **264**, 413 (1994).

[13] H. L. Ju, C. Kwon, Qi Li, R. H. Greene, and T. Venkatesan, Appl. Phys. Lett. **65,** 2108 (1994).

[14] A. Urushibara, Y. Moritomo, T. Arima, A. Asamitsu, G. Kido, and Y. Tokura, Phys. Rev. B **51,** 14 103 (1995).

[15] Y. Tomioka, A. Asamitsu, Y. Moritomo, H. Kuwahara, and Y. Tokura, Phys. Rev. Lett. **74,** 5108 (1995).

[16] P. Schiffer, A. P. Ramirez, W. Bao, and S. -W. Cheong, Phys. Rev. Lett. **75,** 3336 (1995).

[17] Y. Tomioka, A. Asamitsu, Y. Moritomo, and Y. Tokura, J. Phys. Soc. Jpn., **64,** 3626 (1995).

[18] H. Kuwahara, Y. Tomioka, A. Asamitsu, Y. Moritomo, and Y. Tokura, Science **270,** 961 (1995).

[19] A. Asamitsu, Y. Tomioka, Y. Moritomo, T. Arima, and Y. Tokura, Nature **373,** 407 (1995).

[20] A. Asamitsu, Y. Moritomo, R. Kumai, Y. Tomioka, and Y. Tokura, Phys. Rev. B **54,** 1716 (1996).

[21] H. Y. Hwang, S-W. Cheong, N. P. Ong, and B. Batlog, Phys. Rev. Lett. **77,** 2041 (1996).

[22] T. Kimura, Y. Tomioka, H. Kuwahara, A. Asamitsu, M. Tamura, and Y. Tokura, preprint.

[23] T. Arima, Y. Tokura, and J. B. Torrance, Phys. Rev. B **48,** 17 006 (1993).

[24] T. Saitoh, A. E, Bocquet, T. Mizokawa, H. Namatame, A. Fujimori, M. Abbate, Y. Takeda, and M.Takano, Phys. Rev. B **51** 13 942 (1995).

[25] J. Zaanen, G. A. Sawatzky, and J. W. Allen, Phys. Rev. Lett. **55,** 418 (1985).

[26] K. Kubo and N. Ohata, J. Phys. Soc. Jpn. **33,** 21 (1972).

[27] N. Hamada, H. Sawada, and K. Terakura, *Spectroscopy of Mott Insulators and Correlation metals*, edited by A. Fujimori and Y. Tokura, Spinger Verlag. (1995).

[28] N. Furukawa, J. Phys. Soc. Jpn. **64,** 2734 (1995).

[29] N. Furukawa, J. Phys. Soc. Jpn. **64,** 3164 (1995).

[30] Z. Jirak, S. Krupicka, Z. Simsa, M. Dlouha, and Z. Vlatislav, J. Magn. Magn. Mater. **53,** 153 (1985).

[31] H. Yoshizawa, H. Kawano, Y. Tomioka, and Y. Tokura, Phys. Rev. B **52,** 13145 (1995), *ibid.*, J. Phys. Soc. Jpn. **52,** 3626 (1995).

[32] V. Kiryukhin, D. Casa, J. P. Hill, B. Keimer, A. Bigllante, Y. Tomioka, and Y. Tokura, Nature **386,** 813 (1997).

[33] K. Miyano, T. Tanaka, Y. Tomioka, and Y. Tokura, Phys. Rev. Lett. **78,** 4257 (1997).

[34] S. Yamaguchi, Doctor thesis (1997).

[35] A. Wold and R. J. Arnott, J. Phys. Chem. Solids **9,** 176 (1959).

[36] H. Kawano, R. Kajimoto, M. Kubota, and H. Yoshizawa, Phys. Rev. B **53,** 14709 (1996).

[37] To be precise, weak antiferromagnetic peaks are observed in the magnetic neutron scattering up to $x = 0.15$, suggesting canted spin structure.[36]

[38] T. Arima, Y. Tokura, J. Phys. Soc. Jpn. **64,** 2488 (1995).

[39] J. B. Torrance, P. Lacorre, and C. Asavaroengchai, and R. M. Metzger, Physica C **182,** 351 (1991).

[40] S. Yamaguchi, Y. Okimoto, and Y. Tokura, unpublished.

[41] S. Uchida, T. Ido, H. Takagi, T. Arima, Y. Tokura, and S. Tajima, Phys. Rev. B **43**, 7942 (1991).

[42] Y. Taguchi, Y. Tokura, T. Arima, and F. Inaba, Phys. Rev. B **48**, 511 (1993).

[43] F. Inaba, T. Arima, T. Ishikawa, T. Katsufuji, and Y. Tokura, Phys. Rev. B **52**, 2221 (1995).

[44] Y. Okimoto, T. Katsufuji, Y. Okada, T. Arima, and Y. Tokura, Phys. Rev. B **51**, 9581 (1995).

[45] T. Katsufuji, Y. Okimoto, and Y. Tokura, Phys. Rev. Lett. **75**, 3497 (1995).

[46] C. M. Varma, to be published.

[47] A. J. Millis, P. B. Littlewood, and B. I. Shraiman, Phys. Rev. Lett. **75**, 914 (1995).

[48] A. J. Millis, R. Mueller, and Boris I. Shraiman, unpublished.

[49] H. Roder, Jun Zang, and A. R. Bishop, Phys. Rev. Lett. **76**, 1356 (1996).

[50] For example, K. Tamasaku, Y. Nakamura, and S. Uchida, Phys. Rev. Lett. **69**, 1445, (1992); C. C. Homes, T. Timusk, R. Liang, D. A. Bonn, and W. N. Hardy, *ibid* **71**, 1645 (1993).

[51] We adopted a simple Lorentzian form as the dielectric function for the incoherent-part, but used an asymmetric Larenzian for the optical phonon parts to obtain the better fitting.

[52] A. Asamitsu, Y. Moritomo, and Y. Tokura, unpublished.

[53] K. Kumagai and Y. Tokura, unpublished.

[54] Y. Tokura, Y. Taguchi, Y. Okada, Y, Fujishima, T. Arima, K. Kumagai, and Y. Iye, Phys. Rev. Lett. **70**, 2120 (1993).

[55] J.-H. Park, C. T. Chen, S-W. Cheong, W. Bao, G. Meigs, V. Chakarian, and Y. U. Idzerda, Phys. Rev. Lett. **76**, 4215 (1996).

[56] W. F. Brinkman and T. M. Rice, Phys. Rev. B **2**, 4302 (1970).

[57] S. Ishihara, M. Yamanaka, and N. Nagaosa, Phys. Rev. B **56**, 686 (1997).

[58] Y. Tomioka, A. Asamitsu, H. Kuwahara, and Y. Tokura, Phys. Rev. B. **53**, R1689 (1996).

[59] A. Asamistu, Y. Tomioka, and Y. Tokura, Nature **388**, 50 (1997).

[60] Y. Okimoto, T. Katsufuji, T. Ishikawa, A. Urushibara, T. Arima, and Y. Tokura, Phys. Rev. Lett. **75**, 109 (1995), *ibid.* Phys. Rev. B, **55**, 4206.

[61] S. G. Kaplan, M. Quijada, H. D. Drew, D. B. Tanner, G. C. Xiong, R. Ramesh, C. Won, and T. Venkatesan, Phys. Rev. Lett. **77**, 2081 (1996).

[62] S. G. Kim, J. Y. Gu, H. S. Choi, G. W. Park, and T. W. Noh, Phys. Rev. Lett. **77**, 1877 (1996).

[63] T. Katsufuji, T. Tanabe, T. Ishikawa, Y. Fukuda, T. Arima, and Y. Tokura, Phys. Rev. B **54**, R14230 (1996).

[64] S. Ishihara and N. Nagaosa, J. Phys. Soc. Jpn. **66**, 3678 (1997).

Publication list

1. `Optical spectroscopy of the metal-insulator transition in $NdNiO_3$',
T. Katsufuji, Y. Okimoto, and Y. Tokura, Phys. Rev. B **51**, 4830 (1995).

2. `Optical spectra in $(La,Y)TiO_3$: Variation of Mott-Hubbard gap features with change of electron correlation and band filling',
Y. Okimoto, T. Katsufuji, Y. Okada, T. Arima, and Y. Tokura, Phys. Rev. B **51**, 9581 (1995).

3. `Anormalous variation of optical spectra with spin polarization in double-exchange ferromagnet: $La_{1-x}Sr_xMnO_3$',
Y. Okimoto, T. Katsufuji, T. Ishikawa, A. Urushibara, T. Arima, and Y. Tokura, Phys. Rev. Lett. **75**, 109 (1995).

4. `Spectral weight transfer of the optical conductivity in doped Mott insulators',
T. Katsufuji, Y. Okimoto, and Y. Tokura, Phys. Rev. Lett. **75**, 3497 (1995).

5. `Spin-state transition and high-spin polarons in $LaCoO_3$',
S. Yamaguchi, Y. Okimoto, H. Taniguchi, and Y. Tokura, Phys. Rev. B **54**, R2926 (1996).

6. `Bandwidth dependence of insulator-metal transitions in perovskite cobalt oxides',
S. Yamaguchi, Y. Okimoto, and Y. Tokura, Phys. Rev. B **54**, R11022 (1996).

7. `Variation of electronic structure in $La_{1-x}Sr_xMnO_3$ ($0<x<0.3$) as investigated by optical conductivity spectra',
Y. Okimoto, T. Katsufuji, T. Ishikawa, T. Arima, and Y. Tokura, Phys. Rev. B **75**, 4206 (1997).

8. `Local lattice distortion during the spin-state transition in $LaCoO_3$',
S. Yamaguchi, Y. Okimoto, and Y. Tokura, Phys. Rev. B **55**, R8666 (1997).

9. `二重交換系の基本物性',
朝光敦、沖本洋一、十倉好紀、
固体物理 **32**, 258 (1997).

10. `Photonic Phase Control of Magnetic Oxides',
Y. Okimoto, Y. Tokura, Y. Tomioka, Y. Onose, Y. Otsuka, and K. Miyano,
Molecular Crystals and Liquid Crystals, in press.

11. `Charge ordering and disordering transitions $Pr_{1-x}Ca_xMnO_3$ ($x=0.4$) as investigated by optical spectroscopy',
Y. Okimoto, Y. Tomioka, Y. Onose, Y. Otsuka, and Y. Tokura,
Phys. Rev. **B** (Rapid Communication) in press.

12. `Thermally-induced insulator-metal transition in $LaCoO_3$: a view based on Mott transition', Y. Tokura, Y. Okimoto, H. Taniguchi, S. Yamaguchi, T. Kimura, and H. Takagi,
submitted to Phys. Rev. Lett.